JACS Au
AN OPEN ACCESS JOURNAL OF THE AMERICAN CHEMICAL SOCIETY

pubs.acs.org/jacsau
Article

Molecular Mechanisms Underlying Medium-Chain Free Fatty Acid-Regulated Activity of the Phospholipase PlaF from *Pseudomonas aeruginosa*

Rocco Gentile, Matea Modric, Björn Thiele, Karl-Erich Jaeger, Filip Kovacic,* Stephan Schott-Verdugo, and Holger Gohlke*

Cite This: *JACS Au* 2024, 4, 958–973
Read Online

ABSTRACT: PlaF is a membrane-bound phospholipase A_1 from *Pseudomonas aeruginosa* that is involved in remodeling membrane glycerophospholipids (GPLs) and modulating virulence-associated signaling and metabolic pathways. Previously, we identified the role of medium-chain free fatty acids (FFAs) in inhibiting PlaF activity and promoting homodimerization, yet the underlying molecular mechanism remained elusive. Here, we used unbiased and biased molecular dynamics simulations and free energy computations to assess how PlaF interacts with FFAs localized in the water milieu surrounding the bilayer or within the bilayer and how these interactions regulate PlaF activity. Medium-chain FFAs localized in the upper bilayer leaflet can stabilize inactive dimeric PlaF, likely through interactions with charged surface residues, as has been experimentally validated. Potential of mean force (PMF) computations indicate that membrane-bound FFAs may facilitate the activation of monomeric PlaF by lowering the activation barrier for changing into a tilted, active configuration. We estimated that the coupled equilibria of PlaF monomerization-dimerization and tilting at the physiological concentration of PlaF lead to the majority of PlaF forming inactive dimers when in a cell membrane loaded with decanoic acid (C10). This is in agreement with a suggested in vivo product feedback loop and gas chromatography−mass spectrometry profiling results, indicating that PlaF catalyzes the release of C10 from *P. aeruginosa* membranes. Additionally, we found that C10 in the water milieu can access the catalytic site of active monomeric PlaF, contributing to the competitive component of C10-mediated PlaF inhibition. Our study provides mechanistic insights into how medium-chain FFAs may regulate the activity of PlaF, a potential bacterial drug target.

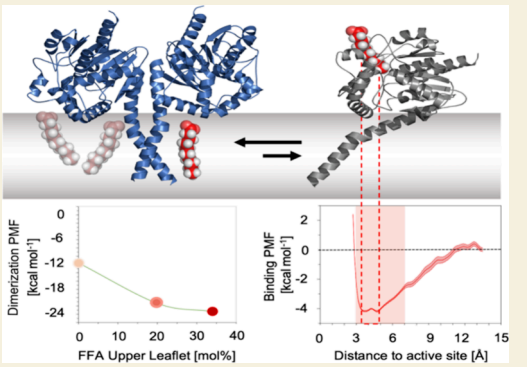

KEYWORDS: *molecular dynamics simulations, membrane, dimerization, tilting, potential of mean force, decanoic acid, inhibition*

1. INTRODUCTION

The Gram-negative bacterium *Pseudomonas aeruginosa* is a human pathogen and a frequent cause of nosocomial infections, affecting primarily immune-compromised patients.[1,2] A large spectrum of virulence factors contributes to the pathogenicity of *P. aeruginosa*.[3] Among these, type A phospholipases (PLA_1) participate in host membrane damage and the modulation of various signaling networks in infected cells.[4,5] PLA_1 hydrolyzes membrane glycerophospholipids (GPLs) at the *sn*-1 position, yielding lysoglycerophospholipids (LGPLs) and free fatty acids (FFAs).[6,7] GPLs are membrane components that are involved in cellular integrity and the regulation of membrane protein function and stability.[8] The alteration of the membrane GPL composition has been linked to biofilm formation, growth phase transition, virulence, and cytotoxicity of *P. aeruginosa*.[1,2,6,9] On the other side, FFA in *P. aeruginosa* acts as a signaling molecule[10] or as the precursor of signal molecules, including hydroxy-alkylquinolines,[11] diffusible signal factors, or oxylipin autoinducer[12] families, which are important for bacterial virulence in the pathogen.[13,14]

Previously, we have shown that *P. aeruginosa* PlaF is a cytoplasmic membrane-bound PLA_1 that contributes to the alteration of the membrane GPL profile and virulence properties of this bacterium.[6] In vitro enzyme activity experiments showed a specificity of PlaF toward GPLs and LGPLs with medium-chain acyl moieties (10−14 carbon atoms), while short- and long-chain GPLs were only poorly hydrolyzed.[6,15] A high-resolution crystal structure of PlaF, combined with homodimerization studies by cross-linking, microscale thermophoresis, and molecular simulations, re-

Received: November 17, 2023
Revised: January 8, 2024
Accepted: January 9, 2024
Published: February 27, 2024

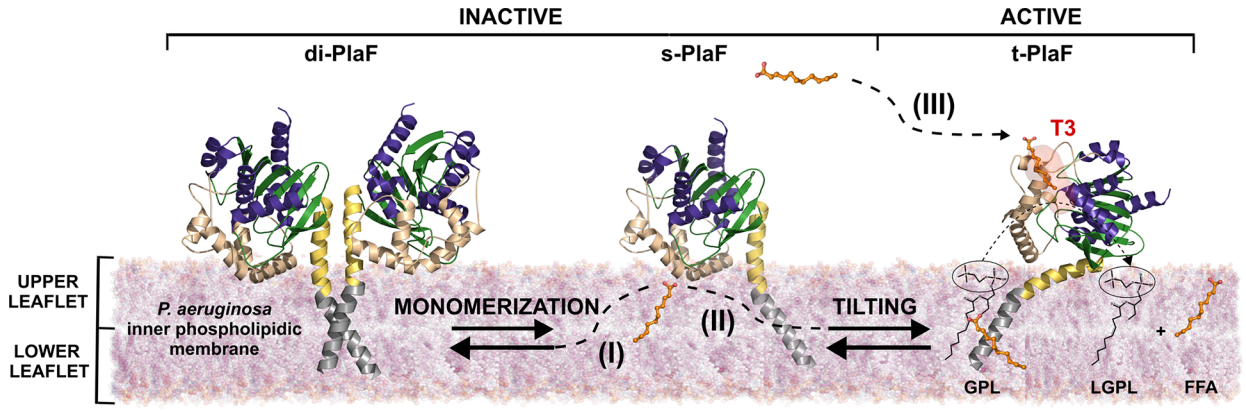

Figure 1. A working model illustrating the possible impact of FFA on the dimer−monomer equilibrium of PlaF and its monomer tilting. PlaF is anchored to the bilayer through a transmembrane (TM) region (gray), predominantly containing hydrophobic residues, and a juxtamembrane (JM) region (yellow) rich in polar and charged residues. The JM domain is in close contact with the polar heads of the phospholipid membrane when PlaF is tilted. The C-terminal catalytic domain points toward the periplasm and is characterized by an α/β-hydrolase fold (green, violet), providing the scaffold for the catalytic triad (Ser, Asp, His) and Arg-Lys-rich lid-like (LL, light brown) domain that presumably interacts with the phospholipid bilayer. PlaF can adopt a dimeric (di-PlaF) or monomeric configuration (s-PlaF), and the monomer can tilt (t-PlaF). The t-PlaF monomer is considered the active form.[6] Lipid bilayer-bound FFA (orange), generated by PlaF from GPL or LGPL, may influence the dimer−monomer equilibrium (I) and/or the tilting transition (II) and/or may enter PlaF from the water milieu (III) through tunnel 3 (T3).

vealed that PlaF can adopt both monomeric and dimeric configurations (Figure 1).[6] However, only the monomeric state of the protein was found to be catalytically active. The crystal structure revealed a homodimer characterized by interactions between the transmembrane (TM) and juxtamembrane (JM) regions between the single monomers. The crystal structure of the PlaF dimer revealed the co-crystallized endogenous ligands undecanoic acid (11A) and tetradecanoic acid (myristic acid, MYR) in the catalytic site of each monomer, with their acyl chains occupying tunnel 1 (T1) pointing toward the dimeric interface.[6]

Free energy computations[16] and experiments have indicated that, at physiological protein concentrations, the equilibrium between the PlaF dimer and the monomers is shifted to the latter side in the cell.[6] In the dimeric form, the entrance of T1 resides more than 5 Å above the membrane's upper leaflet, thus hampering GPL substrate access from the membrane in T1.[6] Interestingly, unbiased molecular dynamics (MD) simulations[17] have shown that the PlaF monomer undergoes a tilting motion in the membrane, bringing the opening of the catalytic tunnel in close vicinity to the membrane, with free energy computations revealing that the tilted state of the monomeric PlaF (t-PlaF) is energetically more favorable than the nontilted state, named split or s-PlaF state (Figure 1).[6] Consequently, it has been suggested that this tilting motion underlies the activation of monomeric s-PlaF by facilitating substrate access to the active site tunnel.[6]

In addition, two other tunnels (T2 and T3) that connect the active site to the surface of PlaF have been identified.[15] Unbiased MD simulations have suggested that MYR, the hydrolysis product of GPL and LGPL, relocates from T3 and reaches the entrance of T1, in agreement with the positions of the co-crystallized ligands MYR and 11A.[6,15] Accordingly, FFAs can reach the membrane bilayer via T1. We have recently shown that medium-chain FFAs, containing 10−14 carbon atoms, inhibit PlaF activity according to a mixed inhibition mode and that they lead to an increase in the PlaF dimer concentration.[6] From our results, we hypothesize that FFAs may inhibit PlaF activity by two mechanisms: (i) allosterically, by impacting the dimer−monomer equilibrium and/or the tilting transition when they are located in the lipid bilayer, and (ii) competitively, by interfering with substrate binding when they enter the active site via T3 from the water milieu mimicking the periplasmic space (Figure 1). However, the detailed molecular mechanisms that govern the PlaF inhibition by FFAs have remained elusive.

Here, we combine unbiased and biased all-atom MD simulations[18] and configurational free energy computations[16] to evaluate the effect of FFAs on the structural dynamics and energetics of the PlaF dimer−monomer transition and monomer tilting and to reveal hot spot PlaF residues that are potentially involved in the interaction with FFAs. Additionally, we pursue free ligand diffusion MD simulations[19] and binding free energy computations[16] of FFAs located in the water phase near the catalytic domain of PlaF. The suggested FFA binding sites in PlaF and their putative roles in inhibition and dimerization were experimentally studied using site-directed mutagenesis and purified PlaF variants reconstituted into small unilamellar vesicles (SUVs) in inhibition and cross-linking assays.

2. RESULTS

2.1. Medium-Chain Fatty Acids Are Detected in *P. aeruginosa* in Free Form and Likely Originate from Glycerophospholipid Hydrolysis

Our previous lipidomics analysis by quadrupole time-of-flight tandem mass spectrometry (Q-TOF MS/MS) revealed that the alteration of the membrane GPL profile of *P. aeruginosa* is linked to the PlaF-mediated degradation of several GPLs, including three GPLs containing medium-chain FAs: phosphatidylglycerol (PG) 24:3, phosphatidylethanolamine (PE) 22:1, and phosphatidylinositol (PI) 26:0.[6] In this study, to evaluate how PlaF modifies the FFA profile and the FFA availability to potentially regulate PlaF activity in the periplasmic space, we analyzed if medium-chain FFAs could be identified in *P. aeruginosa* wild-type (WT) and an isogenic *plaF* mutant (Δ*plaF*) with reduced GPL degrading activity.[6] To achieve this, we extracted FFAs from the cells and supernatant of both strains using organic solvent and

https://doi.org/10.1021/jacsau.3c00725
JACS Au 2024, 4, 958−973

quantified the saturated FFAs with acyl chains of 6−16 carbon atoms by gas chromatography−mass spectrometry (GC-MS). The FFA profile revealed that both *P. aeruginosa* strains produced various intracellularly and extracellularly located saturated FFAs (Figure 2). As anticipated, the long-chain FFAs

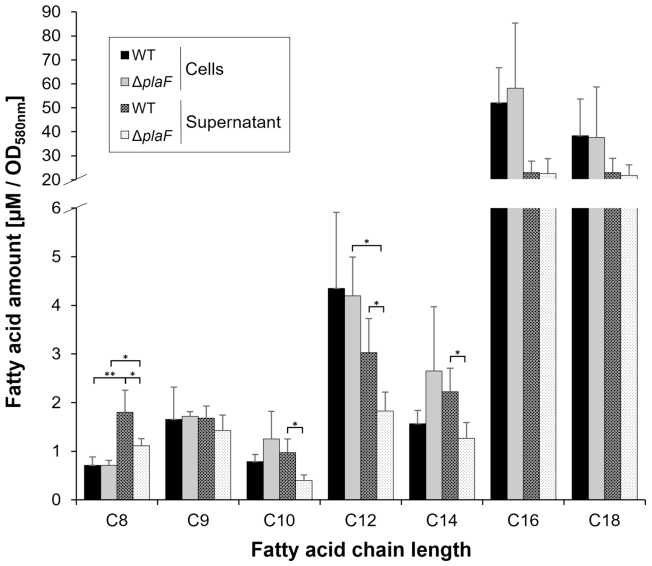

Figure 2. Free fatty acid profile of *P. aeruginosa* WT and Δ*plaF*. Strains were cultivated in LB medium under aeration until the stationary phase, and FFAs were extracted with organic solvent from the cells and supernatant. Quantification of FFAs was performed by GC-MS analysis. Means ± SDs are shown (n = 4 biological replicates). Statistical analysis was performed using the t-test, *p < 0.05 and **p < 0.01; differences between all other data points were not significant.

were the most abundant, while medium-chain FFAs (C8, C9, C10, C12, and C14) accounted for roughly 10−15% of the total FFA amount. No significant differences in the abundance of cell-associated FFAs between the WT and Δ*plaF* strains were observed, suggesting that FFAs released by PlaF are either metabolized or secreted into the supernatant. We identified that medium-chain FFAs, namely octanoic (C8), decanoic (C10), dodecanoic (C12), and myristic (C14) acids, were significantly less abundant (p < 0.05) in the supernatant of Δ*plaF* than in that of WT.

To further explore the possibility that PlaF releases the identified medium-chain FAs from GPLs, we conducted a reanalysis of our published lipidomics results obtained with the Δ*plaF* mutant.[6] Our previous analysis had assessed GPLs at the species level, meaning that only information about the total number of carbon atoms in the acyl chains but not their specific identities had been obtained. Thus, we focused on GPL species with up to 24 carbon atoms in their acyl chains, as they likely contain at least one medium-length acyl chain (Table S1). Our results showed that the *P. aeruginosa* membrane contained 56 different medium-chain length GPLs out of a total of 324 identified GPL species (Table S1). A comparison of the amount of medium-chain length GPLs relative to the total GPL amount in WT and Δ*plaF* revealed that more (20.8%) medium-chain length GPLs were identified in the Δ*plaF* mutant than in the WT strain (12.6%) (Table S2). These results, together with the specificity of PlaF to hydrolyze medium-chain GPLs,[6] suggest that the identified medium-chain FFAs could potentially be generated by the PlaF-catalyzed hydrolysis of GPLs.

The GC-MS analysis revealed an interesting finding: the extracellular octanoic acid amount was nearly double (p < 0.001) that of the intracellular amount in both the WT and Δ*plaF* strains, suggesting that this FFA is predominantly secreted into the supernatant. In contrast, dodecanoic acid, the second FFA identified as a potential PlaF product, was significantly (p < 0.001) more abundant inside the cells of Δ*plaF* than in those of WT. These results show that FFA transport is dependent on their chain length, as has been observed previously for *Escherichia coli* and *Saccharomyces cerevisiae*.[20] This suggests that some FFAs may have a function as extracellularly secreted compounds, such as signaling messengers,[10] while others may be primarily used intracellularly, such as for energy production.[21]

To conclude, the quantification of intracellular and extracellular FFAs is in agreement with our previously determined ability of PlaF to release FFA in vitro from various GPLs[6] and further strengthens the suggested in vivo function of PlaF in degrading GPLs containing medium-length acyl chains.

2.2. Free Fatty Acids in the Membrane May Facilitate the Tilting of PlaF Monomers

To assess the influence of bilayer-bound FFA on PlaF tilting, we performed all-atom unbiased MD simulations[18] of monomeric PlaF inserted into the lipid bilayer loaded with FFA. The orientations of PlaF obtained after splitting the membrane-embedded PlaF dimer (s-PlaF) or the tilted configuration (t-PlaF) obtained with OPM were considered.[22,23] For each PlaF configuration, two membrane systems were examined, in which C10 or C14 was inserted in the upper leaflet, resulting in a DOPE/DOPG/FFA composition of 3:1:1. This system mimics the FFAs bound to the periplasmic leaflet of the inner bacterial membrane, which interacts with the TM, JM, and KR-rich lid-like (LL) domains of PlaF.[6] For each system, 12 replicas were simulated, each 1 μs in length, and the results were compared with those obtained previously with PlaF in an FFA-free bilayer composed of 1,2-dioleoyl-*sn*-glycero-3-phosphoethanolamine (DOPE) and 1,2-dioleoyl-*sn*-glycero-3-phosphoglycerol (DOPG) at a ratio of 3:1, respectively.[6]

When starting from the s-PlaF orientation, a comparable number of transitions to the t-PlaF orientation ("tilting") was observed for the system containing C10 (9/12, 75%) or C14 (10/12, 83%) (Figure 3). These tilting preferences are higher compared to the 50% obtained previously for the system without FFAs.[6] These results indicate that FFAs may facilitate tilting and that, for the tested FFA chain, length has no influence on the tilting preference. When starting MD simulations from the t-PlaF embedded into the C10- or C14-loaded bilayer, no transition to the s-PlaF orientation was observed (Figure 3), even when the MD simulations were prolonged to 2 μs (Figure S1). These results are in agreement with our previous finding that the tilted orientation of PlaF is preferred.[6]

2.3. Free Fatty Acids Favor Monomer Tilting but Disfavor Dimer Dissociation

To determine the effect of FFAs in the upper leaflet on the energetics of the PlaF dimer-to-monomer and s-PlaF-to-t-PlaF transitions, we performed umbrella sampling (US) simulations[24] to compute a PMF.[25] As the chain length showed a

https://doi.org/10.1021/jacsau.3c00725
JACS Au 2024, 4, 958−973

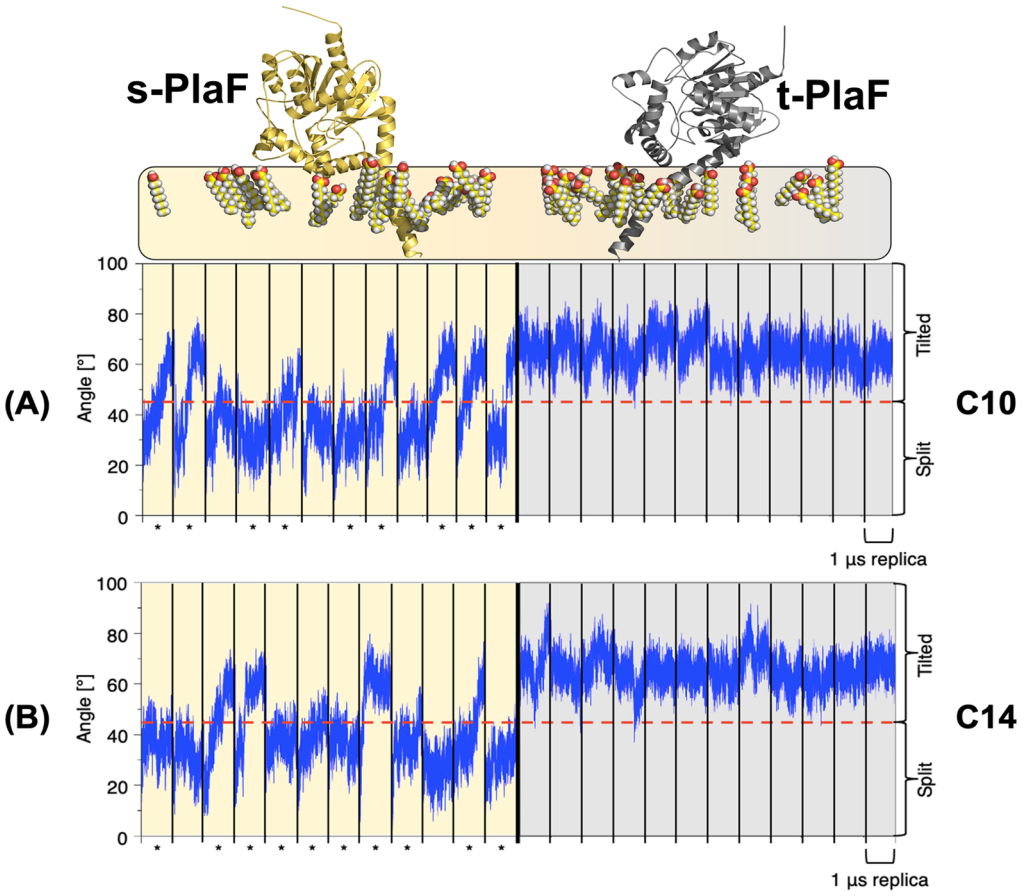

Figure 3. Unbiased MD simulations of monomeric PlaF in the presence of FFA in the upper leaflet. (A) Left (yellow background): time course of the orientation of PlaF with respect to the bilayer starting from s-PlaF in the presence of C10 at a DOPE/DOPG/C10 ratio of 3:1:1. In 9 of the 12 replicas, the s-PlaF adopted a tilted configuration, marked with an asterisk (*). Right (gray background): when starting from t-PlaF, the structure remained tilted in all simulations. As before,[6] this shows a significant tendency of the monomer to tilt (McNemar's $\chi^2 = 6.125$, $p = 0.013$). Tilting is quantified by the angle between the membrane normal and the vector between the center of masses (COM) of C_α atoms of residues 21−25 and residues 35−38 and is assumed to occur if the angle is >45°. (B) Similar to (A), but now with C14 at a DOPE/DOPG/C14 ratio of 3:1:1. In 10 of the 12 replicas, s-PlaF adopted a tilted configuration (marked with *; McNemar's $\chi^2 = 8.100$, $p = 0.004$); t-PlaF did not undergo a transition to s-PlaF.

negligible influence on the tilting behavior in the unbiased MD simulations, we only used a membrane system with a DOPE/DOPG/C10 ratio of 3:1:1. The US simulations were performed as in ref 6, starting from the s-PlaF orientation. The distance between the top of the JM domain, computed as the center of mass (COM) of C_α atoms of residues 33−37, and the membrane center along the membrane normal was used as a reaction coordinate to track the tilting transition. For the dimer-to-monomer transition, we started from the dimer configuration as found in the crystal structure and used the distance between the COM of C_α atoms of residues 25−38 of each PlaF molecule as a reaction coordinate. For the tilting transition, 43 windows were sampled with 800 ns of sampling time each, of which the first 640 ns were discarded as equilibration. Likewise, for the dimer-to-monomer transition, 75 windows were sampled with 800 ns of sampling time each, of which the first 640 ns were discarded as equilibration. In both cases, the kernel densities showed a median overlap of 34.9 ± 1.4% and 32.2 ± 1.5% between contiguous windows, respectively (Figures S2 and S3), which are well-suited for PMF calculations.[26] The standard error of the mean (SEM) was calculated from free energy profiles determined independently every 20 ns from the last 160 ns per window.

The PMF of the titling transition was converged and precise (Figure S2). In the presence of C10 in the bilayer, t-PlaF was preferred over s-PlaF (Figure 4A), which is similar to the results without FFA in the bilayer.[6] However, the global minimum of t-PlaF was lower by ∼4 kcal mol^{-1} in the bilayer containing C10 compared to in the one without C10, indicating that t-PlaF was even more favorable in the presence of C10. Additionally, a local minimum was observed in the system containing C10 instead of a barrier separating the split and tilted PlaF configurations in the system without FFA (Figure 4A). These results are in accordance with the unbiased MD simulations, which indicated that the tilted configuration is preferred and that the transition to it is facilitated in the presence of FFAs.

The PMF for the dimer-to-monomer transition was computed considering two bilayer compositions with 20 mol % and 33.3 mol % of C10 in the upper leaflet. The PMFs were converged and precise (Figures S3 and S4). As in the membrane without FFA,[6] dimeric PlaF was favored over the monomeric state in the presence of C10 in the membrane (Figure 4B). However, FFA stabilized the di-PlaF in a concentration-dependent manner by ∼10 and ∼14 kcal mol^{-1} compared to a system without FFA.

https://doi.org/10.1021/jacsau.3c00725
JACS Au 2024, 4, 958−973

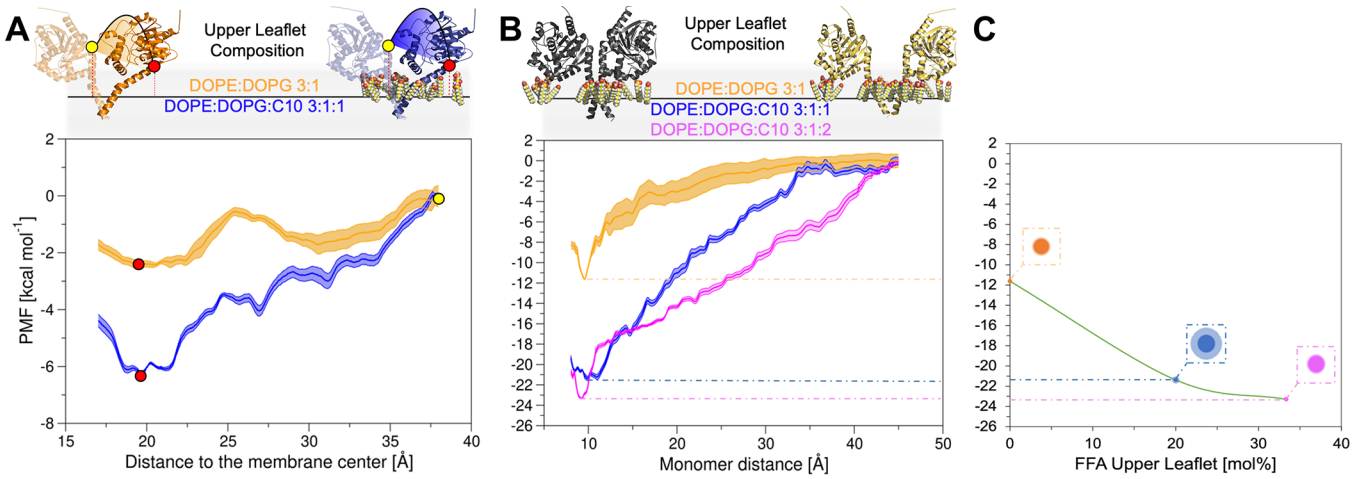

Figure 4. PMFs of monomer tilting and dimer separation. (A) PMF of monomer tilting. The distance along the membrane normal between the COM of C_α atoms of residues 33−37 and the COM of the C18 of the oleic acid moieties of all GPLs in the bilayer was used as a reaction coordinate. Orange: PMF computed for the bilayer consisting of DOPE/DOPG = 3:1 (values were taken from ref 6). Blue: PMF computed here for the bilayer containing C10 in the upper leaflet at a DOPE/DOPG/C10 ratio of 3:1:1. The shaded areas at the curves show the standard error of the mean (SEM). The yellow and red dots indicate s-PlaF and t-PlaF, respectively. (B) PMF of di-PlaF separation. The distance between the COM of C_α atoms of residues 25−38 of each PlaF molecule was used as the reaction coordinate. Orange: PMF values for the bilayer consisting of DOPE/DOPG = 3:1 (values were taken from ref 6). Blue: PMF for the bilayer containing C10 in the upper leaflet at a DOPE/DOPG/C10 ratio of 3:1:1. Magenta: PMF computed for the bilayer containing C10 in the upper leaflet at a DOPE/DOPG/C10 ratio of 3:1:2. The shaded areas show the SEM. The black protein on the top shows the PlaF dimer at a monomer distance of ∼9.9 Å, and the yellow ones show the completely dissociated PlaF at ∼45 Å. (C) PMF values at the respective global minima. This panel shows PMF values at the respective global minima from (B) as a function of the C10 concentration in the upper bilayer leaflet. Dashed lines connect respective points in (B) and (C). The green line connecting the points illustrates a nonlinear correlation between FFA concentration in the upper leaflet and PlaF dimer stabilization. The shaded area around each dot indicates the SEM at the corresponding minimum.

To conclude, the PMF computations demonstrated that the presence of C10 within the upper bilayer leaflet promotes the tilting of s-PlaF, corroborating the findings of our MD simulations (Figure 3A), and C10 exhibits a concentration-dependent stabilizing effect on the PlaF dimer (Figure 4C).

2.4. Estimating the Ratio of Monomeric and Dimeric PlaF in the Cell in the Presence of Free Fatty Acids

Following previous work by us[6,27] and others,[28] we computed from the PMFs of dimer-to-monomer and tilting transitions with an upper leaflet composition of DOPE/DOPG/C10 of 3:1:1 equilibrium constants (K_a = 1.68 × 10^{14} Å^2 (eq S1), K_x = 2.59 × 10^{12} (eq S2), and $K_{tilting}$ = 1.73 × 10^2 (eq S5, Figure S5)) and free energies (ΔG = −17.0 ± 0.2 kcal mol^{-1} (eq S3) and $\Delta G_{tilting}$ = −3.0 ± 0.2 kcal mol^{-1} (eq S6)), taking into account that K_x and ΔG relate to a state of one PlaF dimer in a membrane of 1258 GPLs, according to our simulations setup. Experimentally, a concentration of one PlaF dimer per ∼3786 GPLs in *P. aeruginosa* PlaF-overexpressing cells was determined.[29] However, the concentration in *P. aeruginosa* wild-type (WT) was estimated as 100- to 1000-fold lower.

Under such physiological conditions in the *P. aeruginosa* WT and considering that the equilibria for dimer-to-monomer transition and tilting are coupled, between 2.3% and 7.3% of the PlaF molecules were predicted to be in a monomeric, tilted, catalytically active state in *P. aeruginosa* when 20 mol % C10 were present in the upper leaflet. In the absence of FFAs, between 74% and 96% of the PlaF molecules were predicted to be in a monomeric, tilted, catalytically active state in *P. aeruginosa* WT.[6] Vice versa, in the presence of FFA, 92.7−97.7% of PlaF were in the dimeric configuration, whereas this was only 4−26% in the absence of FFA.[6] The computed increase in the PlaF dimer concentration agrees with our previous biochemical results showing an increased di-PlaF concentration after incubating purified PlaF with C10.[6] Based on these findings, as well as the GC-MS results (Figure 2) that indicated the release of C10 by PlaF in vivo, it is plausible to propose that the degradation of GPLs catalyzed by PlaF is inhibited by the produced C10. This inhibition may serve as a protective product-feedback mechanism to prevent cell membrane damage.

2.5. Hot Spots of di-PlaF−FFA Interactions in the Upper Leaflet Reduce Experimental Dimer Stability When Mutated

To characterize interactions between C10 in the upper leaflet and di-PlaF that may favor dimer formation, we analyzed the trajectories of unbiased MD simulations across 12 replicas. Three-dimensional (3D) density grids representing the probability density of C10 within the membrane led to the identification of states in which C10 was located at a distance of ≤5 Å from the PlaF. To discard short-living di-PlaF−C10 states, we analyzed if the root-mean-square deviation (RMSD) of C10 in two consecutive states was <1.5 Å, indicating that these states encompassed C10 tightly bound to di-PlaF (see the Supplementary results). They were clustered with respect to the minimum distance ε between the clusters starting from ε = 2.0 Å, using the all-atom RMSD as the similarity measure. A gradual increase of ε in 0.5 Å intervals led to a constant population of the largest cluster at ε = 5.0 Å.

The five most populated clusters covered 80.5 ± 1.5% (mean ± SEM) of all systems with C10 close to PlaF and 65.8 ± 1.3% of all systems in a trajectory (Figure 5A). Over these clusters, R187 and R217 with positively charged side chains, E216, containing a negatively charged side chain, and A220 with a nonpolar side chain were identified as the residues mostly interacting with FFA (Figure 5B). These residues are surface-exposed and located in the LL domain, which

https://doi.org/10.1021/jacsau.3c00725
JACS Au 2024, 4, 958−973

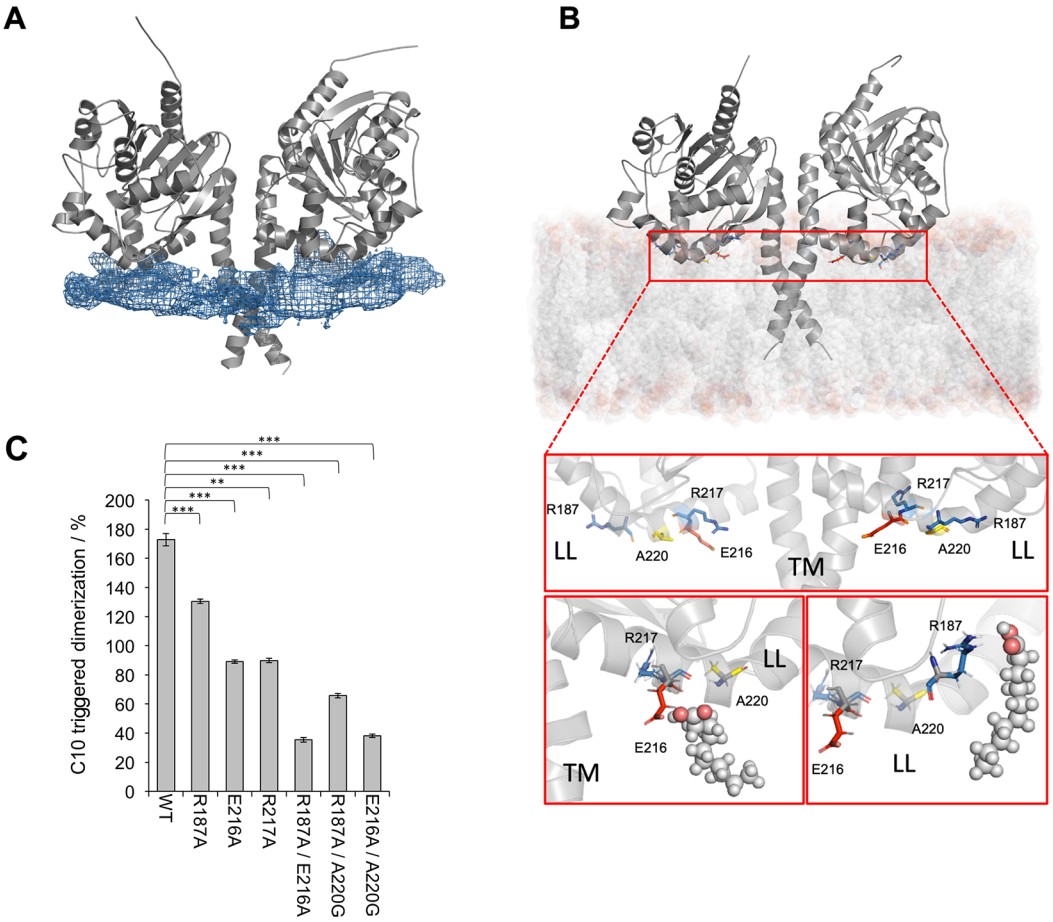

Figure 5. Interaction of C10 located within the upper leaflet with di-PlaF. (A) Average density map of all C10 molecules. 3D density grid illustrating the distribution of all C10 computed with CPPTRAJ.[33] The C10 distributed around both monomers in similar proportions. (B) Hot spots of di-PlaF−C10 interactions. Hot spots were defined as residues with a distance to C10 ≤ 5 Å and where C10 had an RMSD < 1.5 Å with respect to the previous pose. The red box contains the negatively and positively charged hot spots, shown in red and blue sticks, respectively, while nonpolar ones are reported in yellow sticks; LL, the lid-like domain; and TM, the transmembrane domain. Red frames at the bottom show enlarged interaction regions with C10 shown in space-fill format (gray, carbon; and red, oxygen). The left panel indicates the interaction of C10 with E216 and R217. The right panel indicates the interaction of C10 with R187. (C) Effect of mutations in the LL domain on PlaF dimerization. $PlaF_{WT}$ or PlaF variants reconstituted into DOPE/DOPG SUVs were treated with C10 (12 mM) and cross-linker DMP for 2 h at room temperature. SUV reconstituted proteins treated with DMP and DMSO (used as C10 solvent) served as the control without C10. Proteins were separated by SDS-PAGE, followed by Western blot detection of PlaF using anti-His-tag antibodies. The intensities of di-PlaF bands were quantified by ImageJ.[34] The results represent the ratio between C10-untreated and C10-treated samples, shown as mean ± SD (n = 4).

according to the model of di-PlaF in the membrane, interacts with the bilayer.[6]

To experimentally test the role of these residues on PlaF dimerization in the GPL bilayer, we mutated by site-directed mutagenesis each of the three charged residues to alanine to obtain the single variants $PlaF_{R187A}$, $PlaF_{E216A}$, and $PlaF_{R217A}$. Furthermore, a variant with two neutralized charges, $PlaF_{R187A\text{-}E216A}$, and variants with one neutralized charge and C10-interacting A220 mutated to glycine, $PlaF_{R187A\text{-}A220G}$ and $PlaF_{E216A\text{-}A220G}$, were generated. These six PlaF variants and the wild-type PlaF ($PlaF_{WT}$) were produced in *E. coli* and purified by immobilized metal affinity chromatography (IMAC) in the presence of octyl-β-D-glucopyranoside (OG). $PlaF_{WT}$ and the variants purified to homogeneity, as determined by sodium dodecyl−sulfate polyacrylamide gel electrophoresis (SDS-PAGE) (Figure S6A), showed comparable thermal stability as determined by nano differential scanning fluorimetry (nanoDSF) (Table S3). These results indicate that the mutations did not markedly destabilize the protein, as mutations of surface-exposed residues are on average considerably less destabilizing compared to mutations of core residue positions.[30]

Furthermore, we removed OG (Figure S6B) and reconstituted $PlaF_{WT}$ and the variants into SUVs made of DOPE and DOPG, and C10 was added to reach 20 mol %. In the experimental setup, the pH was 8, surpassing the p*K*a value of C10 (6.4), such that C10 was predominantly in a deprotonated and nonmicellized state.[31] In this state, C10 has limited permeability through the phospholipid bilayer, consequently favoring its partitioning within the outer leaflet.[32] This experimental system closely approximates the computational model, rendering it suitable for subsequent comparison with computational data.

A quantitative cross-linking assay (Figure S7) using the bifunctional reagent dimethyl pimelimidate (DMP), which covalently stabilizes dimers, revealed that C10 triggers the formation of $PlaF_{WT}$ dimers (Figure 5C), as shown before.[6] We observed 70% more $PlaF_{WT}$ dimer in the C10-treated sample than in the untreated one. In contrast, all PlaF variants showed a significantly reduced ability to dimerize in the

https://doi.org/10.1021/jacsau.3c00725
JACS Au 2024, 4, 958−973

presence of C10. For single variants, relative amounts of di-PlaF in the C10-treated samples were approximatively equal to those in the untreated samples. In double-point variants, less di-PlaF in the C10-treated samples than in the C10-untreated samples was observed. These results indicate that residues predicted by MD simulations to interact with C10 within the bilayer play an important role in C10-triggered PlaF dimerization.

2.6. Free Fatty Acids in the Aqueous Milieu Interact with t-PlaF Primarily via Entering T3

Subsequently, we investigated if C10 from the aqueous milieu could directly bind to PlaF without prior entry into the bilayer. To explore this, we conducted all-atom unbiased MD simulations of free ligand diffusion (fldMD) that were 1 μs in length. Such simulations have been previously used to predict the binding modes of molecules.[19] t-PlaF was embedded in a bilayer with the composition DOPE/DOPG = 3:1, and 10 molecules of C10 were added to the water phase, resulting in concentrations of 30 mM in the solvation box. This concentration, which was higher than the experimentally used one, was chosen to increase the probability of observing events of C10 binding to and dissociating from t-PlaF. As this concentration is above the critical micelle concentration (CMC) of C10,[35] we monitored by visual inspection of the trajectories that no C10 aggregates formed.

We performed 12 replicas, and binding and unbinding events of C10 were monitored (Figure S8). We identified a C10 as "bound" if it was within a distance of <5 Å from the T3 entrance, defined as the COM of residues K170, Q234, and Y236, and had an RMSD < 1.5 Å to the previous position within the trajectory (see the Supplementary results).[15] Density maps of C10 around t-PlaF showed that C10 tended to gather in T3 (Figure 6A), as is also supported by the finding that T3 is involved in 8.61% of the total binding events of C10 to t-PlaF (Figure S8). In most events, the acyl chain of C10 entered T3 first (Figure 6B), which is compatible with the mostly hydrophobic interior of T3.[15] T3 has previously been suggested to play a role in the catalytic cycle by relocating substrates during catalysis.[15] Thus, the identified C10−PlaF interactions in T3 may influence enzyme activity. Furthermore, it has been hypothesized that FFA released from the GPL may diffuse to the periplasmic space via T3;[15] therefore, it is feasible that C10 may also enter PlaF via the same path.

2.7. Tail-First Access of C10 into T3 Is Energetically Favorable

As a prerequisite to computing the energetics of the binding of C10 to the T3 of PlaF, we validated if C10 access via its tail is favorable. We applied steered MD (sMD) simulations[37] to pull C10 from the bound state obtained during fldMD simulations to the unbound state in which C10 is located outside T3 in an aqueous milieu. We did not use a trajectory from the fldMD simulations, as the C10 tail did not insert deeply enough into T3 to reach the catalytic site. The transition pathway was later used to define reference points for US simulations to compute a PMF of C10 egress. A bound C10 of replica 4 of the fldMD simulations was chosen as a representative pose (Tables S4 and S5 (t-PlaF(III): CAP-1127)). The terminal carbon atom of C10 was considered for pulling from a distance of 3.4 Å to the catalytic oxygen of S137 to 13.1 Å, where it was in the solvent. The C10 was pulled through four consecutive virtual points (Figure 7A,B and Movie S1), which were chosen such that the entire egress pathway was covered, as described before.[15] The

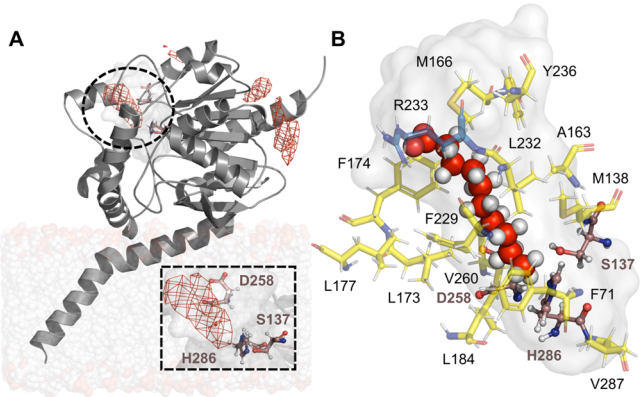

Figure 6. Free ligand diffusion MD simulations reveal access of C10 molecules to T3. (A) 3D density grids (red mesh) showing the probability density of C10 around t-PlaF. All C10 were considered in the 3D density grid calculations, and the contour level was set as 1 standard deviation above the mean value (1σ). T3, computed using CAVER 3.0,[36] is depicted as a light gray surface. The region (black dashed circle) around the catalytic triad (S137, D258, and H286, indicated as brown sticks) is shown in the blow-up image (black dashed rectangle). (B) A representative binding mode of C10 located within T3 from the most populated cluster that comprises 51.8 ± 0.3% of all bound C10 configurations. T3 was calculated using CAVER 3.0[36] and is presented as a light gray surface. Carbon and hydrogen atoms of C10 are depicted as red and gray spheres, respectively. The catalytic triad is illustrated as brown sticks, and the T3 residues are shown as yellow sticks, except for R233, which is represented with blue sticks.

distance between the pulled C-terminal carbon atom and the virtual point was used as a reaction coordinate. The pulling was repeated 50 times for each step, and the work done was computed as a function of the reaction coordinate, as done in previous work[15] (Figure 7A). By applying Jarzynski's relation (eq 1),[38] the work was related to the free energy difference between the respective two states along the transition pathway.

$$\overline{e^{-W/kT}} = e^{-\Delta F/kT} \quad (1)$$

The sMD trajectory whose work versus reaction coordinate profile was closest to the Jarzynski average was identified as the most favorable transition pathway[15] (Figure 7B). Its end point provided the starting point for the sMD simulations in the next part of the transition pathway. As a result, the transition pathway was close to the lowest free energy pathway of C10 egress from the catalytic site to the aqueous milieu. Overall, this approach is similar to sampling the unbinding trajectories of ligands from proteins before applying Jarzynski's relation,[39−41] but it uses piecewise sMD simulations along the pathway to account for the curvilinear tunnel. A total of 1.15 μs of sMD simulation time was used.

PMFs were computed from US simulations along the sMD-determined transition pathway[24] and postprocessed with WHAM[42,43] to evaluate the energetics of C10 egress. As a reaction coordinate, the distance between the terminal carbon atom of C10 to the side-chain oxygen of catalytic S137 was used. In total, 29 windows were sampled with 260 ns of sampling time each, of which the first 100 ns were discarded as equilibration. The kernel density showed a median overlap of 33.6 ± 3.1% between contiguous windows, which is well-suited for PMF calculations.[26] The PMF of C10 egress was converged and precise (Figure S9). It revealed the presence of an energetic global minimum associated with the bound state I,

https://doi.org/10.1021/jacsau.3c00725
JACS Au 2024, 4, 958−973

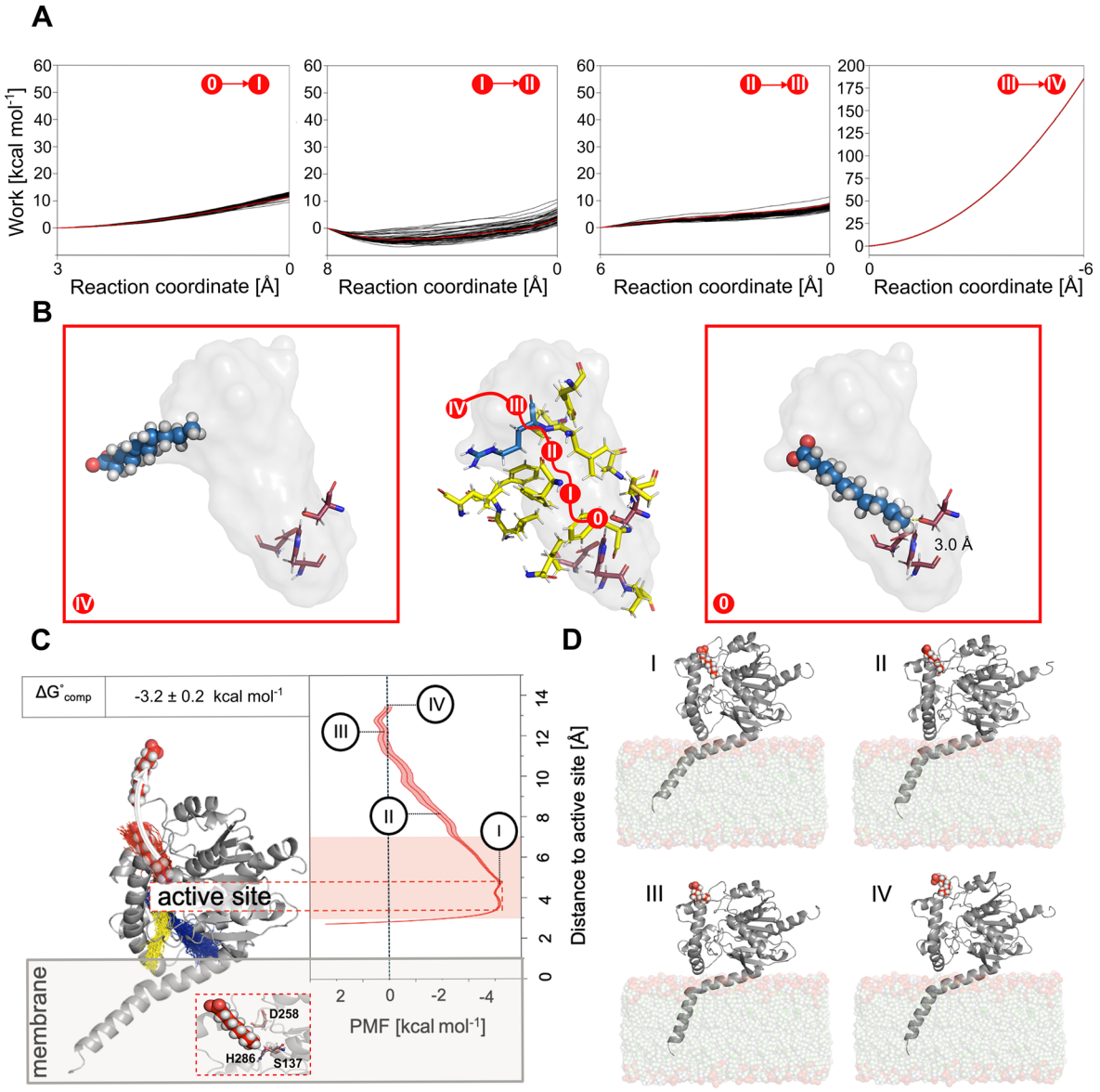

Figure 7. Binding free energy of C10 to T3, as determined by sMD and umbrella sampling. Work distributions (black lines) were obtained from 50 replicas of sMD simulations. (A) C10 pulled out of T3 via its tail. C10 was first pulled from the bound position (0) to point I. A replica closest to the Jarzynski average (red line) was considered as the starting point for the next pulling, I → II. This pulling continued until IV, after which C10 was completely pulled out of T3. The reaction coordinate denotes the distance to the target point. (B) The starting point and the final point of the pulling are illustrated. (0) is the initial bound position with a distance of 3.0 Å between the catalytic Ser oxygen and the terminal methyl group of the fatty acid. (IV) is the final position, with the terminal methyl group of the fatty acid being pulled out of the tunnel. The catalytic triad residues are represented with purple sticks. The gray T3 tunnel surface was computed with CAVER 3.0.[36] (C) PMF profile of C10 egress through T3 in the t-PlaF configuration and (D) corresponding states. (C) The entrance of T3 (red) is located >35 Å above the membrane, pointing into the aqueous milieu; T1 and T2 (blue and yellow, respectively) point to the membrane. C10 is pulled from the bound state through T3 into the water phase mimicking the periplasmic space in the cell. The catalytic site is marked with a dotted red box. The red-shaded area around the curve represents the SEM. The red-shaded box corresponds to the integration limits used to calculate K_{eq} (eq 2) to determine $\Delta G_{comp}°$. (D) Corresponding states during the C10 egress. State I: starting position of C10 (in the bound state). State II: C10 tail reaches half of the tunnel. State III: C10 tail is close to the tunnel interface with the periplasmic space. State IV: C10 reaches the end of T3. The C10 molecule is surrounded by water.

which is ∼4 kcal mol^{-1} more favorable than the partially bound states II and III as well as the unbound state IV (Figure 7C,D). The computed binding free energy ($\Delta G_{comp}°$)[25] of −3.2 ± 0.2 kcal mol^{-1} indicates that tail-first access of C10 to T3 is energetically favorable. These results further strengthen the suggestion that the entry of C10 from the aqueous milieu to T3 and its binding close to S137 could prevent a substrate (GPL or LGPL) from reaching the catalytic site, thereby competitively inhibiting PlaF activity.[15]

2.8. Tryptophan Substitutions in T3 Are Suggested to Interfere with C10 Access

To validate the prediction that T3 is the preferred pathway for C10 entering PlaF from the water phase, we used the previously characterized Trp substitutions F229W and L177W within T3 that caused tunnel constriction (Table 1) without affecting protein thermostability.[15] This strategy has previously been employed to block tunnels of dehalogenases[44] and PlaF[15] with respect to substrate access. T3 could be

https://doi.org/10.1021/jacsau.3c00725
JACS Au 2024, 4, 958−973

Table 1. Effect of Single Mutations on C10 Binding to T3 in t-PlaF WT and Two Variants Identified from fldMD Simulations

PlaF	occurrence[a]	average bottleneck radius[b,c]	C10 binding events[d]	effective binding free energy[e]
WT	27.75	2.29 ± 0.32	8.61	−16.5 ± 0.5
F229W	24.78	1.67 ± 0.31	6.90	−17.9 ± 0.6
L177W	28.37	1.70 ± 0.34	5.42	−21.3 ± 1.5

[a]In %; frequency of occurrence of T3 in CAVER. [b]Data was calculated with CAVER using a probe radius of 1.2 Å. [c]In Å; the average and SD are given. [d]In %; frequency that describes the number of T3-bound frames compared to the total number of frames. [e]In kcal mol^{-1}; the average and SEM are given.

identified at a similar occurrence rate (Table 1) in PlaF$_{WT}$ and both PlaF variants; therefore, these Trp variants were suitable for experimentally studying the binding of C10 from the aqueous milieu to the T3.

MD simulations of the free ligand diffusion of C10 were performed to observe binding events to T3 in the two PlaF variants, applying the same criteria as described for PlaF$_{WT}$. The results indicated a reduction in the number of C10 binding events to T3 compared to PlaF$_{WT}$ to 6.90% in PlaF$_{F229W}$ and 5.42% in the PlaF$_{L177W}$ variant (Table 1 and Figures S8, S10, and S11). 3D density grids of C10 molecules from the fldMD simulation trajectories indicated that the C10 occurrences around the two engineered Trp sites were reduced compared to PlaF$_{WT}$, but the orientation and the depth by which C10 immerses into T3 were similar among all three proteins (Figure 8A).

To further evaluate the effect of the Trp substitutions on C10 interactions within T3, we computed binding effective free energies using the molecular mechanics Poisson−Boltzmann surface area (MM-PBSA) method with an implicit membrane model.[45,46] For this, frames from the fldMD simulations with bound C10 were used. The computations were converged, as evidenced by the comparison between the first and second halves of the trajectories (Figure S12). Across 12 different replicas, we identified 24, 19, and 14 trajectories in which C10 molecules were bound to the T3 of PlaF$_{WT}$, PlaF$_{F229W}$, and PlaF$_{L177W}$, respectively. The results revealed that C10 molecules bind to T3 more favorably in the Trp variants (ΔG_{eff} (PlaF$_{F229W}$) = −17.9 ± 0.6 kcal mol^{-1}; ΔG_{eff} (PlaF$_{L177W}$) = −21.3 ± 1.5 kcal mol^{-1}) than in WT (ΔG_{eff} (PlaF$_{WT}$) = −16.5 ± 0.5 kcal mol^{-1}) (see Table 1 and Figure 8A). Such a more prevalent bound state may explain the reduced number of binding events of C10 to T3 of Trp variants (Table 1). The more favorable binding in the variants likely arises from better interactions of the lipophilic tail of C10 with the bulky side chain of Trp than with the WT residues.

To experimentally investigate the effect of the Trp substitutions in T3 on the inhibition of PlaF by C10, we produced PlaF$_{WT}$, PlaF$_{F229W}$, and PlaF$_{L177W}$ using the *P. aeruginosa* expression system,[6] purified the proteins in the presence of dodecyl-β-D-maltoside (DDM) using IMAC,[15] and reconstituted them in DOPE/DOPG SUVs using a methodology similar to that employed for the LL domain variants. Subsequent inhibition studies by varying the concentration of C10 while keeping the protein and substrate concentrations constant revealed half-maximal inhibitory concentrations (IC_{50}) for PlaF$_{WT}$ and the Trp variants (Figure 8B). Results show reduced IC_{50} values for the Trp variants compared to that of WT, indicating a stronger inhibitory effect of C10 on the Trp variants in comparison to PlaF$_{WT}$. These experimental results are in agreement with the computed binding effective free energies (Table 1) and further strengthen the role of T3 in the binding of C10.

3. DISCUSSION

In this study, we combined molecular simulations at the atomistic level with biochemical experiments to examine how the interaction of medium-chain FFAs with PlaF regulates PlaF activity. Using in vivo, in vitro, and computational analyses, we previously established a model[6] according to which the homodimerization of catalytically active PlaF monomers leads to PlaF inhibition, a process induced by medium-chain (C10−C14) FFAs. Following monomerization, PlaF reorients in the bilayer by tilting,[6] which is essential for its activation, as it allows membrane-bound GPL substrates to reach the active site.[15] Here, we further refined the model of PlaF activity regulation by assessing the impact of C10 located (i) in the GPL bilayer or (ii) in the aqueous milieu surrounding the GPL bilayer on the dimer−monomer transition and the tilting as well as on substrate access to the active site.

3.1. Effect of FFAs in the GPL Bilayer on PlaF

Our MD simulations and PMF computations revealed that C10 in the GPL bilayer exerts a stabilizing effect on the inactive di-PlaF configuration, in accordance with findings from covalent cross-linking experiments.[6] This stabilization likely arises from favorable interactions between FFAs localized in the upper bilayer leaflet and predominantly positively charged residues located in the PlaF LL domain, which is close to the upper leaflet in the di-PlaF configuration. Mutagenesis experiments and DMP cross-linking studies using purified proteins functionally validated the predictions by showing that single-charged residue-to-alanine variants exhibited reduced dimerization compared to PlaF$_{WT}$. Notably, higher C10 concentrations were predicted to stabilize di-PlaF more, which led us to hypothesize that multiple interactions between membrane-localized FFAs and residues within the LL domain occur simultaneously. We validated this hypothesis by using double variants carrying combinations of residues identified as FFA interaction sites in our MD simulations. These double variants showed a more strongly reduced PlaF dimerization than single-point variants. Furthermore, our MD simulations and PMF computations indicated that C10 promotes the t-PlaF configuration and facilitates the tilting process. The latter might be attributed to a potential reduction in membrane viscosity caused by the addition of FFAs as membrane components.[47] Still, considering the physiological conditions in the *P. aeruginosa* WT and that the equilibria for the dimer-to-monomer transition and tilting are coupled, between 2.3% and 7.3% of the PlaF molecules were predicted to be in a monomeric, tilted, catalytically active state in *P. aeruginosa* when 20 mol % C10 was present in the upper leaflet. This is more than 10-fold less than in *P. aeruginosa* WT in the absence of C10.[6] The observed impact of FFAs located in the GPL bilayer on the transitions of PlaF likely contributes to the noncompetitive/allosteric component of a mixed inhibition kinetics mechanism previously demonstrated for FFA acting on PlaF.[6]

3.2. Effect of FFAs in Aqueous Milieu on PlaF

Medium-chain FFAs were co-crystallized in the active site of PlaF, and they competed with the substrate according to

https://doi.org/10.1021/jacsau.3c00725
JACS Au 2024, 4, 958−973

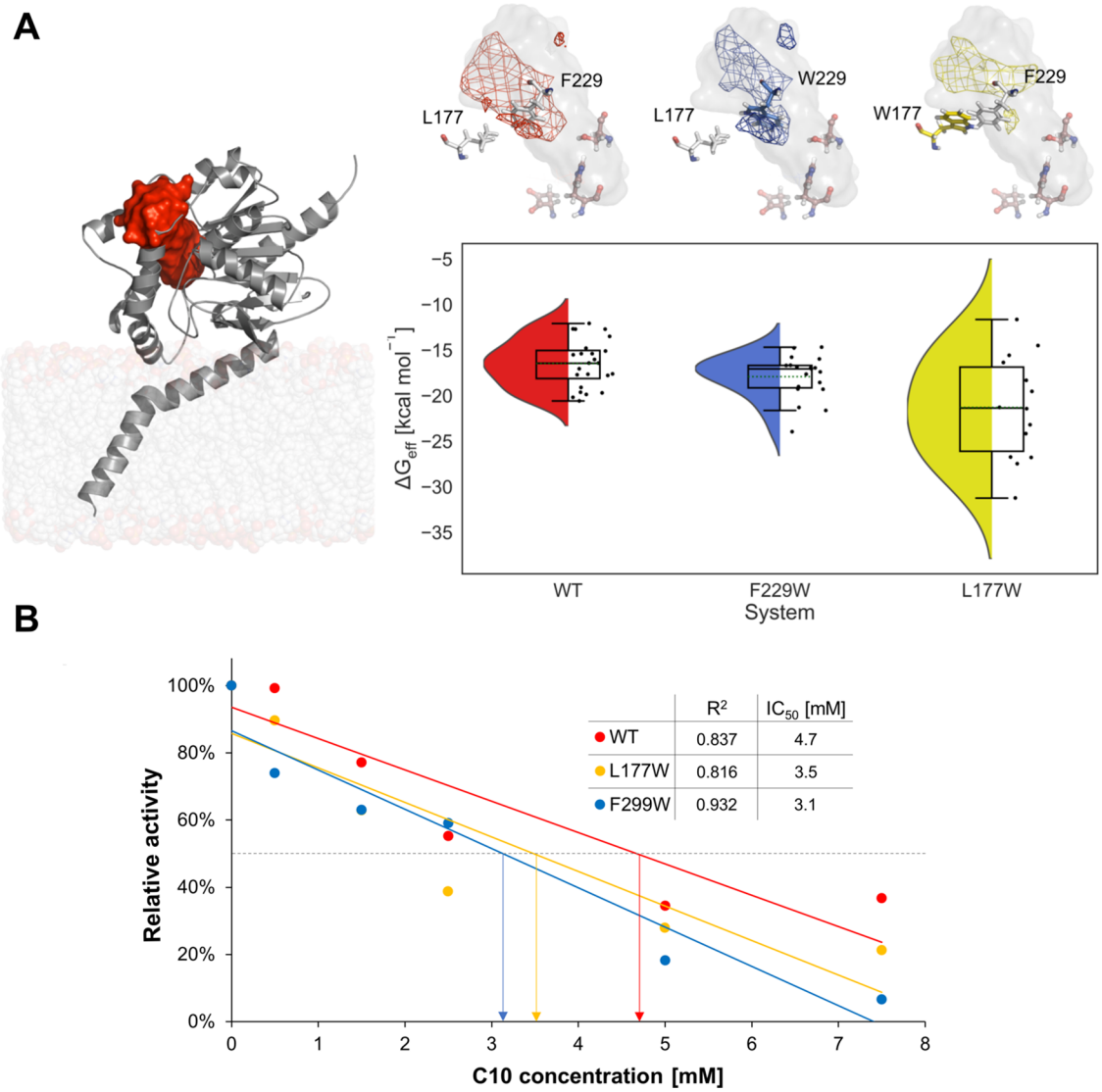

Figure 8. Effect of T3 mutations on FFA binding to PlaF. (A) Binding of FFA to T3 in $PlaF_{WT}$ and the Trp variants. Left: The $PlaF_{WT}$ T3 is shown as a red surface in t-PlaF (gray cartoon). Top right: C10 3D density grids based on fldMD simulations. The contour level is set as 1σ. T3 is depicted as a gray surface, and the catalytic triad is shown as brown sticks. The substitution sites are shown as white sticks, except for the included tryptophans, which are represented with blue sticks for $PlaF_{F229W}$ and yellow sticks for $PlaF_{L177W}$. The density grids are colored accordingly, except for the WT, which is shown in red. Bottom right: Violin plot indicating the distribution of the binding effective energies of FFAs to T3. The inner box of the box plot represents the interquartile range, with the horizontal black line indicating the median. The dotted green line represents the mean, and the vertical black line shows the rest of the distribution, excluding points determined to be outliers when they fall outside 1.5× the interquartile range. (B) Inhibitory effect of C10 on $PlaF_{WT}$ and the PlaF variants. Linear plots of relative activities (sample without C10 was set to 100%) and C10 at concentrations in the range of 0−7.5 mM. Linear correlation coefficients (R^2) and IC_{50} values are indicated. The results represent the mean of initial reaction velocities measured six times using esterase substrate (*p*-NPB) and proteins purified in the presence of DDM.

previous inhibition kinetics results.[6] To scrutinize if C10 localized in the water phase of a bilayer-bound PlaF can interact with the enzyme such that substrate binding is impacted, we performed fldMD simulations. These simulations revealed that C10 can bind to the active monomeric t-PlaF via T3, which was previously identified to connect the active site of PlaF with the surrounding water milieu.[15] C10 favors tail-first access and can reach close to the catalytic triad with its tail. In such a configuration, C10 may potentially interfere with substrate binding, which could explain the experimentally determined competitive effect of C10 on PlaF. We next studied by fldMD simulations previously characterized PlaF variants with genetically engineered bulky Trp residues in T3 ($PlaF_{F229W}$ or $PlaF_{L177W}$).[15] The simulations revealed that binding events for C10 occurred less frequently in either single variant, as might have been expected due to the narrowed T3. Interestingly, binding effective free energy computations revealed that C10 binds stronger to T3 in the variants, i.e., the less frequent binding events there result from C10 being bound longer in T3. These predictions are in line with biochemical studies revealing that inhibition of the PlaF variants reconstituted in SUVs by C10 was enhanced compared to $PlaF_{WT}$. Together, our results indicate that T3 is involved in the inhibition of PlaF by C10 in the water phase.

3.3. Possible Physiological Relevance of FFA-Mediated PlaF Inhibition

Comparative GC-MS profiling of FFAs secreted by *P. aeruginosa* Δ*plaF* and the wild-type cells revealed that PlaF

https://doi.org/10.1021/jacsau.3c00725
JACS Au 2024, 4, 958−973

can release medium-chain FFAs, including C10 and C14, from GPLs as in vitro substrates. This result corroborates our suggestion that PlaF exerts multiple physiological functions[48] through GPL degradation.[6] We observed that the chain length of the FFAs has a minor impact on the tilting transition. This leads to the hypothesis that the noncompetitive/allosteric component of a mixed inhibition kinetics mechanism of PlaF is similarly influenced by other medium-chain FFAs as described here for C10, although further investigations are needed to validate this. At physiologically relevant concentrations in *P. aeruginosa*, we estimated that PlaF predominantly exists as inactive di-PlaF in the presence of FFAs. These results, together with the predicted function of T3 for C10 inhibition, strongly suggest that product feedback regulation of PlaF catalytic activity may be important for in vivo PlaF-mediated GPL degradation and membrane remodeling.

In conclusion, our study provides detailed mechanistic insights into the impact of medium-chain FFAs on the in vitro regulation of PlaF activity. While likely similar mechanisms are active in vivo, this needs to be experimentally validated in the future. Disentangling FFA-mediated activity regulation of the integral membrane protein PlaF is challenging, as FFAs may bind into the protein, interact with the protein from the bilayer, and change bilayer properties (e.g., viscosity). Our MD simulations and free energy computations provide evidence that the interplay of these mechanisms serves as a regulatory factor governing PlaF function. Studying membrane proteins in near-native conditions within GPL vesicles, as was done here, shall help to disentangle these complex relationships further. Our results should help understand the regulatory role of FFAs present in the periplasm or inner bacterial membrane on PlaF and eventually other single TM helix spanning membrane proteins because FFAs are among the most common regulators of protein function.[49] They also open up new perspectives on how to inhibit PlaF, which has been suggested as a promising target for developing new antibiotics against *P. aeruginosa*.[6]

4. MATERIALS AND METHODS

4.1. Gas Chromatography–Mass Spectrometric (GC-MS) Analysis of FAs Extracted from *P. aeruginosa*

P. aeruginosa PA01 (wild-type, WT) and the Δ*plaF* mutant were cultivated overnight (37 °C, lysogeny broth (LB) medium, agitation), and the cells were separated from the supernatant. This was followed by the chloroform/methanol extraction of FFAs, derivatization of FFAs with *N*-methyl-*N*-(trimethylsilyl)trifluoroacetamide, and quantification by GC-MS, as described in ref 50.

4.2. Preparation of Starting Structures

The crystal structure of the PlaF dimer is available in the Protein Data Bank (PDB ID: 6I8W).[51] The last five residues of the C-terminus of each monomer missing in the structure were added using MODELLER,[52] and all small molecule ligands were removed. The dimer was oriented in the membrane using the PPM server (di-PlaF).[22] From that, the "split" s-PlaF$_A$ configuration of chain A was generated by removing chain B from the dimer orientation. Additionally, chain A was oriented using the PPM server, resulting in the tilted configuration t-PlaF. These three starting configurations, di-PlaF, s-PlaF, and t-PlaF, were embedded into a DOPE/DOPG = 3:1 membrane[53] and solvated using PACKMOL-Memgen.[54,55] The membrane composition resembled that of the native inner membrane of Gram-negative bacteria.[53]

Free fatty acids (FFA) of different chain lengths were added as upper-leaflet components in the protonated form[56] in two different concentrations; here, "upper" refers to the leaflet pointing to the periplasmic space. A distance of at least 15 Å between the protein or membrane and the solvent box boundaries was kept. To obtain a neutral system, counterions were added that replaced solvent molecules (0.15 M KCl). The generated systems are summarized in Table S4. The sizes of the resulting systems was ∼140 000 atoms for s-PlaF and t-PlaF and ∼185 000 atoms for di-PlaF.

4.3. Unbiased Molecular Dynamics Simulations of PlaF Monomers

The GPU particle mesh Ewald implementation from the AMBER21 suite of molecular simulation programs[57] with the ff14SB[58] and Lipid14/17 force fields[59,60] for the protein and the membrane lipids were used, respectively; water molecules and ions were parametrized using the TIP3P model[61] and the Li and Merz 12-6 ions parameters.[62,63] For the monomer configurations (s-PlaF and t-PlaF), 12 independent simulations 1 μs in length were performed (Table S4). Covalent bonds to hydrogens were constrained with the SHAKE algorithm[64] in all simulations, allowing the use of a time step of 2 fs. Details of the thermalization of the simulation systems are given below. All unbiased MD simulations showed stable protein structures and membrane phases, as evidenced by electron density calculations (Table S4 and Figures S13–S16).

4.4. Relaxation, Thermalization, and Production Runs of the PlaF Monomers

An initial minimization step was performed with the CPU code pmemd.[65] Each minimization was organized in four steps of 1000 cycles each, for a total of 4000 cycles of minimization. Afterward, each minimized system was thermalized in one stage from 0 to 300 K over 25 ps using the NVT ensemble and the Langevin thermostat,[66] and the density was adapted to 1.0 g cm^{-3} over 975 ps using the NPT ensemble with a semi-isotropic Berendsen barostat[67] with the pressure set to 1 bar. The thermalization and equilibration were performed with the GPU code pmemd.[65] There were three density equilibration steps with a total time of 4 ns. The sum of the thermalization, density adaptation, and equilibration took 5 ns.

For each replica, 1 μs of production run using the GPU code pmemd was performed in the NPT ensemble at a temperature of 300 K using the Langevin thermostat[66] and a collision frequency of 1 ps^{-1}. To avoid noticeable distortions in the simulation box size, semi-isotropic pressure scaling using the Berendsen barostat[67] and a pressure relaxation time of 1 ps was employed by coupling the box size changes along the membrane plane.[68]

4.5. Analysis of MD Trajectories of the PlaF Monomer

The trajectories were analyzed with CPPTRAJ.[33] As in ref 6, the angle between the membrane normal and the vector between the COMs of C_α atoms of residues 21–25 and residues 35–38 was calculated to describe the tilting of monomeric PlaF.

4.6. PMF and Free Energy Calculation of Dimer Dissociation

For calculating a configurational free energy profile (PMF) of dimer separation, 71 intermediate states were generated by separating one chain of the dimer along the membrane plane in steps of 0.5 Å. The generated structures represented the separation process of the PlaF dimer. To sample configurations along the chain separation in a membrane environment, each intermediate state was embedded into a membrane of approximately 157 × 157 Å by using PACKMOL-Memgen[55] (see section 4.2 and Table S4 for the composition of the systems). Each intermediate state was minimized, thermalized, and equilibrated following the protocol that has already been described (sections 4.2 and 4.3).

Umbrella sampling simulations were performed starting from each equilibrated intermediate state by restraining the initial distance between chains in every window with a harmonic potential using a force constant of 4 kcal mol^{-1} Å^{-2};[24] the distance between the COM of C_α atoms of residues 25–38 of each monomer was used as a reaction coordinate value r. Independent MD simulations that were 800 ns in length were each started from each intermediate state, resulting in a total simulation time of 56.8 μs. r was recorded every 2 ps and postprocessed with the Weighted Histogram Analysis Method

https://doi.org/10.1021/jacsau.3c00725
JACS Au 2024, 4, 958–973

implementation of WHAM 2.0.9,[42] removing the first 640 ns as an equilibration phase of the system. The error was estimated by considering the last 160 ns only and by calculating the standard error of the mean from eight independent free energy profiles that were determined every 20 ns during this time. The overlap between contiguous windows and the convergence of the PMFs were validated (Figures S3 and S4). The association free energy was estimated from the obtained PMF following the membrane two-body derivation[28] and our previous work[6,27] (eqs S1−S4).

4.7. PMF and Free Energy Calculation of Monomer Tilting

The initial conformations used in every window for calculating the PMF of the monomer tilting were obtained from the first microsecond of the MD simulations of replica 2 of s-PlaF in the Tilt1 system (Table S4). Oriented as in the di-PlaF crystal structure, the monomer spontaneously tilted. The distance d along the z-axis between the COM of C_α atoms of residues 33−37 of the monomer with the membrane center was used to select 40 intermediate tilting configurations, as was done already with a standard membrane composition.[6] The starting conformations were extracted from the representative trajectory, taking the respective snapshots where d showed the least absolute deviation to the average value obtained by binning d in windows that were 0.5 Å in width and with an evenly distributed separation of 0.5 Å. d was restrained for every configuration by a harmonic potential with a force constant of 4 kcal mol^{-1} Å^{-2}, and sampling was performed for 800 ns per window. d values were obtained every 2 ps and analyzed as described above. The error was estimated in the same way as for the dimerization. The overlap between contiguous windows and the convergence of the PMF were validated (Figure S2). The free energy of monomer tilting was estimated from the obtained PMF following protocols explained in previous works[6,25] (eqs S5−6).

The dissociation and tilting equilibrium constants as well as the proportion of PlaF dimer to monomer in a live cell of *P. aeruginosa* were calculated in the same way as in ref 6; see also the Supporting Information.

4.8. Density Maps of Free Fatty Acids Binding to di-PlaF in the Membrane

The structure of the PlaF dimer was embedded in a phospholipid membrane with the composition DOPE/DOPG = 3:1 following the protocol described in section 4.1. C10 fatty acids were added as membrane upper-leaflet components in the protonated configuration.[56] The final composition of the upper leaflet was DOPE/DOPG/C10 = 3:1:1. Unbiased MD simulations of the system were performed following the protocol used for the monomers (see sections 4.2 and 4.3). From the obtained trajectories, all FFA binding poses were identified in which FFAs had an RMSD < 1.5 Å to the previous frame (see the Supplementary results) and were located at most 5 Å away from the protein. These binding poses were clustered using the hierarchical agglomerative (bottom-up) algorithm implemented in CPPTRAJ,[33] using the minimum distance ε between the clusters as the cluster criterion. Starting from ε = 2.0 Å, we gradually increased ε in 0.5 Å intervals until the population of the largest cluster remained unchanged (ε = 5.0 Å). We calculated the 3D density maps of the fatty acids considering all atoms using the grid function available in CPPTRAJ using a grid spacing of 1.5 Å.[33] We applied a contour level of 1σ (one standard deviation above the mean value).

4.9. fldMD to Study C10 FFA Binding from the Water Phase to t-PlaF

t-PlaF was embedded in a phospholipid membrane with the composition DOPE/DOPG = 3:1 following the protocol described in section 4.1. To investigate the binding of FFAs to PlaF, 1 μs long MD simulations of the free diffusion of FFA molecules located in the water phase were performed to investigate their binding to t-PlaF. The FFAs were assumed to be in their deprotonated configuration, resulting in a concentration of ∼30 mM in the corresponding solvation box. The eventual formation of aggregates was checked by visual inspection of the trajectories. Twelve replicas that were 1 μs in simulation length were run for each system. The minimization, thermalization, equilibration, and production schemes were like the ones performed in sections 4.2 and 4.3.

4.10. Simulated Extraction of Fatty Acids through T3

MD simulations were performed using the GPU implementation of the AMBER 21 molecular simulation package,[55] employing the same protocol as in sections 4.3 and 4.4. To extract an FFA from T3 into the periplasmic space, we selected a bound FFA (Table S4 (t-PlaF(III): CAP-1127)) of replica 4 of the fldMD simulations as a representative pose. We pulled it by its terminal carbon atom from the catalytic center to the tunnel's exit using constant velocity sMD simulations with a constant velocity of 1 Å ns^{-1} and a force constant of 5 kcal mol^{-1} Å^{-2}.[37,41] Pulling simulations at low velocities have been used with lipids to calculate free energy profiles.[15,69] Using low pulling rates, the lipids have time to adapt to energetically favorable conformations during the extraction process. T3 was divided into consecutive fragments connected to T3 pulling points generated by the COM of specific amino acid residues (Table S5). We performed 50 replicas for each pulling simulation to identify the lowest energy pathway. The work was computed as a function of the reaction coordinate. The computed work was further related to the free energy difference between two states of the pulling simulation by applying Jarzynski's relation (eq 1).[38] ΔF is the free energy difference between two states, which is connected to the work W done on the system. k is the Boltzmann constant, and T is the absolute temperature of the system. The replica closest to the Jarzynski average[38] was considered to describe the lowest free energy pathway and provided the starting point for the next pulling stage, as was done in ref 15. This procedure results in a faster convergence of PMF profiles subsequently computed along the pathway, decreasing the overall computations needed.[39]

4.11. Umbrella Sampling Simulations and PMF Calculations

To understand the energetic contribution associated with the binding of C10 molecules to T3, PMFs were computed based on umbrella sampling, taking structures from the sMD simulations (see section 4.10) as starting points. As a reaction coordinate, the distance of the terminal carbon atom of the FFA to the hydroxyl oxygen of S137 of the active site was used. Consecutive positions of the FFA from the bound state to the periplasmic space, as determined in section 4.10, were considered reference points, defining the umbrella windows. To achieve sufficient overlap between the umbrella windows, distances between reference points of 0.5 Å were used. The length of T3 and the size of the FFA can vary. Therefore, for sampling the egress of the bound fatty acid, different numbers of windows were required for the tunnel. The FFA was restrained by harmonic potentials to the reference points using a force constant of 5 kcal mol^{-1} Å^{-2}. To achieve sufficient convergence of the PMF profile (Figure S9), each window was sampled for 260 ns, of which the last 160 ns were used to calculate the PMF. Distance values were recorded every 2 ps and processed with WHAM.[42] The PMFs were evaluated for convergence by checking the change in the free energy profile with increasing sampling time in steps of 20 ns (Figure S9).

4.12. Absolute Binding Free Energy from the PMF

The absolute binding free energy of fatty acids to PlaF was determined from the computed PMF using an approach modified[15] from Chen and Kuyucak.[26] The PMF was integrated along the reaction coordinate (eq 2) to calculate an association (equilibrium) constant (K_{eq}):

$$K_{eq} = \pi r^2 \int_{\text{periplasm}}^{\text{active site}} e^{-W(\xi)/k_B T}\, d\xi \tag{2}$$

where r is the maximum bottleneck radius of the respective tunnel, which was determined by CAVER analysis,[15,36] πr^2 is the maximum cross-sectional area of the tunnel, $W(\xi)$ is the PMF at a specific value of the reaction coordinate, k is the Boltzmann constant, and T is the absolute temperature at which the simulations were performed. The integration limits describe the bound state. A reaction coordinate >7

https://doi.org/10.1021/jacsau.3c00725
JACS Au 2024, 4, 958−973

Å was considered as an unbound state and, for this reason, was not included in the integration.

K_{eq} was then transformed to the mole fraction scale (K_x). For (un)binding to the solution, a standard state of 1 M is considered[25] (eq 3).

$$K_x = K_{eq}\frac{1\ \text{mol}}{1\ \text{L}} = K_{eq}\frac{1}{1660\ \text{Å}^3} \quad (3)$$

From K_x, the difference in the standard free energy (eq 4) between the bound and unbound states (ΔG_{comp}°) of a single substrate molecule was calculated.

$$\Delta G_{comp}^{\circ} = -RT\ \ln(K_x) \quad (4)$$

4.13. Predicting Mutations to Modify Access of the Free Fatty Acid to T3

To verify the prediction that FFA can bind to T3 and, thereby, inhibit PlaF, we intended to alter the geometry of T3 by introducing small-to-tryptophan substitutions of tunnel-lining residues, following an approach that has already been pursued.[15] The selected residues were substituted to tryptophan using FoldX,[70] and the stability of the PlaF variants was evaluated in terms of the change in the folding free energy ($\Delta\Delta G$) with respect to the wild-type[71] (Table S6). Single and double amino acid substitutions were performed 10 times for each residue or residue couple, and the results were averaged. If the average $\Delta\Delta G$ was >3 kcal mol^{-1}, the substitution was considered destabilizing[72] and was not further pursued. To check if the proposed substitutions would modify the tunnel geometry, the bottleneck radius and the tunnel length of the variant tunnels were calculated using CAVER 3.0[36] (Table S6). The COMs of the catalytic residues S137 and H286 were defined as the starting points of the search, as done in our previous work.[15] The probe radius was set to 1.2 Å.

Mutant fldMD simulations and binding free energy calculations of C10 to T3 were performed by following the same protocols described for the wild-type PlaF.

4.14. MM-PBSA Calculations of Free Fatty Acid Binding to t-PlaF from the Water Phase

To pinpoint the most likely binding epitopes, we generated 3D density grids to map the location of each fatty acid. Conformations that were stably bound (as defined in section 4.8) were then clustered to extract the most representative binding poses. Subsequently, we conducted MM-PBSA (molecular mechanics Poisson−Boltzmann surface area) calculations to determine the binding effective energy of FFAs binding to t-PlaF from the water phase. These calculations were performed for both the WT PlaF and the proposed mutants, utilizing the trajectories from fldMD. FFA binding poses were identified as those exhibiting an RMSD < 1.5 Å compared to the previous frame (as described in section 2.5). Additionally, these poses were required to be located within 5 Å of the entrance of T3.

To compute the average binding effective energy of each FFA interacting with t-PlaF within the ensemble of C10 frames, we employed MMPBSA.py.[46] This was done using dielectric constants of 1.0 for the protein, 80.0 for the solvent, and 15.0 for the membrane.[73] A heterogeneous dielectric model was used to represent the membrane; the implicit membrane model using spline fitting (memopt = 3) was employed for these calculations.[45]

4.15. Cloning, Site-Directed Mutagenesis, Expression, and Purification

Molecular biology methods were performed following previously described procedures.[6] For obtaining PlaF variants of the lid-like domain, site-directed mutagenesis of *plaF* (*pa2949*) was carried out using the Quik-Change PCR method with the Phusion DNA polymerase and the pET_pa2949 plasmid.[74] Similarly, mutants located in the T3 tunnel were generated through site-directed mutagenesis on pBBR1MCS-3_pa2949.[29] Successful site-directed mutagenesis was confirmed by DNA sequencing.

For the production of PlaF and the lid-like domain variants, *E. coli* BL21(DE3) cells transformed with the respective expression vectors were grown overnight at 37 °C in LB medium[75] supplemented with ampicillin (100 μg/mL).[74] These cultures were used to inoculate an expression culture in "autoinduction" medium (terrific broth medium containing 0.04% lactose (w/v) and 0.2% glucose (w/v)) supplemented with ampicillin (100 μg/mL) to an OD_{600} (initial optical density measured at 600 nm) of 0.01. The cultures were then grown for 24 h at 37 °C and harvested by centrifugation at 6750 × *g* and 4 °C for 15 min.

For the production of the PlaF and T3 tunnel variants, transformed *P. aeruginosa* PA01 cells were grown overnight at 37 °C in LB medium supplemented with tetracycline (100 μg/mL).[6] These cultures were used to inoculate an expression culture in LB medium supplemented with tetracycline (100 μg/mL) to an initial OD_{600} of 0.05. The cultures were grown at 37 °C until reaching OD = 2 and were then harvested by centrifugation at 6750 × *g* and 4 °C for 15 min.

The total membrane fraction isolated by ultracentrifugation was solubilized with Triton X-100,[6] and the proteins were purified using Ni-NTA IMAC and buffers supplemented with 20 mM OG for the lid-like protein variants and 0.25 mM DDM for the T3 tunnel protein variants. For biochemical analysis, the proteins were transferred to Tris-HCl buffer (100 mM, pH = 8) supplemented with the respective detergents. The PlaF protein and its variants were analyzed by SDS-PAGE under denaturation conditions on a 12% (v/v) gel.[76]

4.16. Reconstitution of Proteins into GPL SUVs

Small unilamellar vesicles (SUV) were constructed and used for reconstitution according to a modified protocol.[77] The GPLs used, namely 1,2-dioleoyl-*sn*-glycero-3-phosphoglycerol (DOPG) and 1,2-dioleoyl-*sn*-glycero-3-phosphoethanolamine (DOPE), were dissolved in chloroform (Avanti Polar Lipids, Alabaster, U.S.).

To produce 2.6 μmol of SUVs for protein reconstitution and 64.9 μmol of SUVs for fatty acid reconstitution, DOPE and DOPG were mixed in a 1:1 ratio in a glass reaction vessel. The GPLs were dried under a gentle stream of nitrogen and by centrifugation under a vacuum for 20 min. Subsequently, HEPES buffer (20 mM, pH = 8, 100 mM NaCl) was added to the dried GPLs, and they were incubated for 10 min at room temperature. The GPLs were then vortexed and sonicated for 2 min. OG and DDM were added to the SUVs at a detergent/SUV ratio of 2:1 or 1:1 (mol/mol) to destabilize the SUVs, respectively. After destabilization of the SUVs, the samples were incubated with rotation for 1 h to ensure complete equilibration of the detergent with the lipids.

FAs were mixed with the respective detergent-destabilized SUVs to achieve a GPL-to-FA ratio of 5:1 (mol/mol). Proteins were mixed with the respective detergent-destabilized SUVs with or without C10 to achieve a GPL-to-protein mass ratio of 20:1. Final protein concentrations were 1000 nM to achieve dimerization. To remove the detergent, approximately 20 activated polystyrene Bio-Beads were added to the reconstitution solution, which was incubated for 1 h with rotation at room temperature.

4.17. Cross-Linking Assays

In vitro cross-linking using the bifunctional cross-linking reagent dimethyl pimelimidate (DMP) was performed, as previously described.[6] Briefly, 30 μL of proteins reconstituted into SUVs were incubated with 1.8 μL of decanoic acid (332 mM) and 18 μL of freshly prepared DMP in phosphate buffer saline (pH = 7.4, 150 mM) for 2 h at room temperature to ensure partitioning of C10 to the bilayer. The cross-linking reaction was terminated with 15 μL of stop solution (50 mM Tris-HCl, 1 M glycine, 150 mM NaCl, pH = 8.3).

4.18. Enzyme Activity Assay

The esterase activities of the SUV-reconstituted PlaF and T3 variants were determined at 37 °C using *p*-nitrophenyl butyrate (*p*-NPB) as a substrate, following the protocol previously described.[78] The protein (5 μL) was mixed with 93 μL of a freshly prepared 1 mM *p*-NPB solution and 2 μL of C10 dissolved in dimethyl sulfoxide (DMSO). Final protein concentrations were 130.22, 280.52, and 77.22 nM for $PlaF_{WT}$, $PlaF_{L177W}$, and $PlaF_{F299W}$, respectively, and final FA concentrations were 0.5, 1.5, 2.5, 5, and 7.5 mM. Activities were determined by measuring the release of *p*-nitrophenol spectrophoto-

https://doi.org/10.1021/jacsau.3c00725
JACS Au 2024, 4, 958−973

metrically during 1 h at 410 nm. Inhibition was assessed by calculating the relative activities of the inhibited samples in comparison to the activity of the sample without C10, which was set to 100%. IC_{50} values were estimated from linear plots, as was done in ref 79.

4.19. Thermal Stability

PlaF and variants were loaded into the measuring capillaries (Prometheus NT.Plex nanoDSF grade standard capillary chips) and were heated from 20 to 90 °C (heating rate of 1 °C/min), and the intrinsic protein fluorescence was recorded at 330 and 350 nm using the Prometheus NT.Plex nanoDSF device (NanoTemper, Munich, Germany).

4.20. SDS-PAGE and Western Blotting

Proteins were analyzed by SDS-PAGE under denaturation conditions on 12% (w/v) gels, as described previously.[74] The proteins were transferred from the SDS-PAGE gel to the polyvinylidene difluoride membranes by Western blotting and were detected using anti-His(C-term)-HRP antibodies (Invitrogen), as described previously.[80]

4.21. Detergent Quantification

We performed detergent quantification following established procedures.[81] To do so, 25 μL of each protein sample, 50 μL of 5% phenol, and 125 μL of 96% sulfuric acid were pipetted in a 1.5 mL Eppendorf tube. Samples were vortexed and incubated at 90 °C for 5 min. After the samples had cooled to room temperature, 150 μL were transferred to a 96-well microtiter plate, and absorbance was measured at 490 nm. The calibration curve was prepared with the respective detergent in the same manner as the samples.

■ ASSOCIATED CONTENT

Data Availability Statement

The AMBER21 source code is available at http://ambermd.org/. Input coordinate, parameter and topology, and input parameter files as well as scripts to analyze the simulation data are available at http://dx.doi.org/10.25838/d5p-53. All experimental data is included in the manuscript.

Supporting Information

The Supporting Information is available free of charge at https://pubs.acs.org/doi/10.1021/jacsau.3c00725.

Supplementary results (PMF and free energy calculations, determination of the binding mode models for C10 FFAs), six supplementary tables, 16 supplementary figures, and a description for Movie S1 (PDF)

Movie S1: extraction of a C10 fatty acid molecule via the tail from the bound position 289 inside T3 of t-PlaF using sMD simulations (MP4)

■ AUTHOR INFORMATION

Corresponding Authors

Filip Kovacic − *Institute of Molecular Enzyme Technology, Heinrich Heine University Düsseldorf, Forschungszentrum Jülich GmbH, 52425 Jülich, Germany*; Email: f.kovacic@fz-juelich.de

Holger Gohlke − *Institute for Pharmaceutical and Medicinal Chemistry, Heinrich Heine University Düsseldorf, 40225 Düsseldorf, Germany; Institute of Bio- and Geosciences (IBG-4: Bioinformatics), Forschungszentrum Jülich GmbH, 52425 Jülich, Germany*; orcid.org/0000-0001-8613-1447; Email: gohlke@uni-duesseldorf.de

Authors

Rocco Gentile − *Institute for Pharmaceutical and Medicinal Chemistry, Heinrich Heine University Düsseldorf, 40225 Düsseldorf, Germany*; orcid.org/0009-0007-1391-4986

Matea Modric − *Institute of Molecular Enzyme Technology, Heinrich Heine University Düsseldorf, Forschungszentrum Jülich GmbH, 52425 Jülich, Germany*

Björn Thiele − *Institute of Bio- and Geosciences (IBG-2: Plant Sciences and IBG-3: Agrosphere), Forschungszentrum Jülich GmbH, 52425 Jülich, Germany*

Karl-Erich Jaeger − *Institute of Molecular Enzyme Technology, Heinrich Heine University Düsseldorf, Forschungszentrum Jülich GmbH, 52425 Jülich, Germany; Institute of Bio- and Geosciences (IBG-1: Biotechnology), Forschungszentrum Jülich GmbH, 52425 Jülich, Germany*

Stephan Schott-Verdugo − *Institute of Bio- and Geosciences (IBG-4: Bioinformatics), Forschungszentrum Jülich GmbH, 52425 Jülich, Germany*

Complete contact information is available at: https://pubs.acs.org/10.1021/jacsau.3c00725

Author Contributions

R.G.: computational investigation, analysis, and visualization. M.M. and B.T.: experimental investigation, analysis, and visualization; S.S.-V.: supervision and analysis. K.-E.J., F.K., and H.G.: conceptualization, supervision, analysis, funding, resources, and project management. The manuscript was written with the contributions of all authors. All authors have given approval for the final version of the manuscript.

Notes

The authors declare no competing financial interest.

■ ACKNOWLEDGMENTS

This study was funded by the Deutsche Forschungsgemeinschaft (DFG, German Research Foundation), Project 267205415/CRC1208, grant to F.K. and K.-E.J. (subproject A02) and H.G. (subproject A03). We thank Muttalip Caliskan (IMET, HHU Düsseldorf) for the help with the fatty acid quantification. We are grateful for the computational support by the "Zentrum für Informations und Medientechnologie" at the Heinrich Heine Universität Düsseldorf and the computing time provided by the John von Neumann Institute for Computing (NIC) to H.G. on the supercomputer JUWELS at the Jülich Supercomputing Centre (JSC) (user IDs: HDD18; plaf).

■ REFERENCES

(1) Gellatly, S. L.; Bains, M.; Breidenstein, E. B. M.; Strehmel, J.; Reffuveille, F.; Taylor, P. K.; et al. Novel roles for two-component regulatory systems in cytotoxicity and virulence-related properties in *Pseudomonas aeruginosa*. *AIMS Microbiol.* **2018**, *4* (1), 173−191.

(2) Gellatly, S. L.; Hancock, R. E. *Pseudomonas aeruginosa*: new insights into pathogenesis and host defenses. *Pathog. Dis.* **2013**, *67* (3), 159−73.

(3) Hauser, A. R. *Pseudomonas aeruginosa*: so many virulence factors, so little time. *Crit. Care Med.* **2011**, *39* (9), 2193−4.

(4) Flores-Diaz, M.; Monturiol-Gross, L.; Naylor, C.; Alape-Giron, A.; Flieger, A. Bacterial sphingomyelinases and phospholipases as virulence factors. *Microbiol. Mol. Biol. Rev.* **2016**, *80* (3), 597−628.

(5) Hurley, B. P.; McCormick, B. A. Multiple roles of phospholipase A2 during lung infection and inflammation. *Infect. Immun.* **2008**, *76* (6), 2259−72.

(6) Bleffert, F.; Granzin, J.; Caliskan, M.; Schott-Verdugo, S. N.; Siebers, M.; Thiele, B.; et al. Structural, mechanistic, and physiological insights into phospholipase A-mediated membrane phospholipid degradation in *Pseudomonas aeruginosa*. *eLife* **2022**, *11*, e72824.

(7) Chwastek, G.; Surma, M. A.; Rizk, S.; Grosser, D.; Lavrynenko, O.; Rucinska, M.; et al. Principles of membrane adaptation revealed through environmentally induced bacterial lipidome remodeling. *Cell. Rep.* **2020**, *32* (12), 108165.
(8) Hishikawa, D.; Hashidate, T.; Shimizu, T.; Shindou, H. Diversity and function of membrane glycerophospholipids generated by the remodeling pathway in mammalian cells. *J. Lipid Res.* **2014**, *55* (5), 799−807.
(9) Benamara, H.; Rihouey, C.; Abbes, I.; Ben Mlouka, M. A.; Hardouin, J.; Jouenne, T.; et al. Characterization of membrane lipidome changes in *Pseudomonas aeruginosa* during biofilm growth on glass wool. *PLoS One.* **2014**, *9* (9), No. e108478.
(10) Fernandez-Pinar, R.; Espinosa-Urgel, M.; Dubern, J. F.; Heeb, S.; Ramos, J. L.; Camara, M. Fatty acid-mediated signalling between two *Pseudomonas* species. *Environ. Microbiol. Rep.* **2012**, *4* (4), 417−23.
(11) Dulcey, C. E.; Dekimpe, V.; Fauvelle, D. A.; Milot, S.; Groleau, M. C.; Doucet, N.; et al. The end of an old hypothesis: the *Pseudomonas* signaling molecules 4-hydroxy-2-alkylquinolines derive from fatty acids, not 3-ketofatty acids. *Chem. Biol.* **2013**, *20* (12), 1481−91.
(12) Martínez, E.; Orihuela, C. J.; Campos-Gomez, J. *Pseudomonas aeruginosa* Secretes the Oxylipin Autoinducer Synthases OdsA and OdsB via the Xcp Type 2 Secretion System. *J. Bacteriol.* **2022**, *204* (7), No. e0011422.
(13) Liu, L.; Li, T.; Cheng, X.-J.; Peng, C.-T.; Li, C.-C.; He, L.-H.; et al. Structural and functional studies on *Pseudomonas aeruginosa* DspI: implications for its role in DSF biosynthesis. *Sci. Rep.* **2018**, *8* (1), 3928.
(14) Songer, J. G. Bacterial phospholipases and their role in virulence. *Trends Microbiol.* **1997**, *5* (4), 156−61.
(15) Ahmad, S.; Strunk, C. H.; Schott-Verdugo, S. N.; Jaeger, K. E.; Kovacic, F.; Gohlke, H. Substrate access mechanism in a novel membrane-bound phospholipase A of *Pseudomonas aeruginosa* concordant with specificity and regioselectivity. *J. Chem. Inf. Model.* **2021**, *61* (11), 5626−43.
(16) Chipot, C. Free energy calculations applied to membrane proteins. *Methods Mol. Biol.* **2008**, *443*, 121−44.
(17) Lotz, S. D.; Dickson, A. Unbiased molecular dynamics of 11 min timescale drug unbinding reveals transition state stabilizing interactions. *J. Am. Chem. Soc.* **2018**, *140* (2), 618−28.
(18) Monje-Galvan, V.; Warburton, L.; Klauda, J. B. Setting up all-atom molecular dynamics simulations to study the interactions of peripheral membrane proteins with model lipid bilayers. *Methods Mol. Biol.* **2019**, *1949*, 325−39.
(19) Frieg, B.; Gremer, L.; Heise, H.; Willbold, D.; Gohlke, H. Binding modes of thioflavin T and congo red to the fibril structure of amyloid-beta(1−42). *Chem. Commun. (Camb).* **2020**, *56* (55), 7589−92.
(20) Salvador López, J. M.; Van Bogaert, I. N. A. Microbial fatty acid transport proteins and their biotechnological potential. *Biotechnol. Bioeng.* **2021**, *118* (6), 2184−201.
(21) Zhang, Y. M.; Rock, C. O. Membrane lipid homeostasis in bacteria. *Nat. Rev. Microbiol.* **2008**, *6* (3), 222−33.
(22) Lomize, M. A.; Pogozheva, I. D.; Joo, H.; Mosberg, H. I.; Lomize, A. L. OPM database and PPM web server: resources for positioning of proteins in membranes. *Nucleic Acids Res.* **2012**, *40* (D1), D370.
(23) Lomize, M. A.; Lomize, A. L.; Pogozheva, I. D.; Mosberg, H. I. OPM: orientations of proteins in membranes database. *Bioinformatics.* **2006**, *22* (5), 623−5.
(24) Torrie, G.M.; Valleau, J.P. Nonphysical sampling distributions in Monte Carlo free-energy estimation: Umbrella sampling. *J. Comput. Phys.* **1977**, *23* (2), 187−99.
(25) Doudou, S.; Burton, N. A.; Henchman, R. H. Standard free energy of binding from a one-dimensional potential of mean force. *J. Chem. Theory Comput.* **2009**, *5* (4), 909−18.
(26) Chen, P. C.; Kuyucak, S. Accurate determination of the binding free energy for KcsA-charybdotoxin complex from the potential of mean force calculations with restraints. *Biophys. J.* **2011**, *100* (10), 2466−74.
(27) Pagani, G.; Gohlke, H. On the contributing role of the transmembrane domain for subunit-specific sensitivity of integrin activation. *Sci. Rep.* **2018**, *8* (1), 5733.
(28) Johnston, J. M.; Wang, H.; Provasi, D.; Filizola, M. Assessing the relative stability of dimer interfaces in g protein-coupled receptors. *PLoS Comput. Biol.* **2012**, *8* (8), No. e1002649.
(29) Bleffert, F.; Granzin, J.; Gohlke, H.; Batra-Safferling, R.; Jaeger, K. E.; Kovacic, F. *Pseudomonas aeruginosa* esterase PA2949, a bacterial homolog of the human membrane esterase ABHD6: expression, purification and crystallization. *Acta Crystallogr. F Struct. Biol.* **2019**, *75* (4), 270−7.
(30) Teufl, M.; Zajc, C. U.; Traxlmayr, M. W. engineering strategies to overcome the stability-function trade-off in proteins. *ACS Synth Biol.* **2022**, *11* (3), 1030−9.
(31) Namani, T.; Walde, P. From decanoate micelles to decanoic acid/dodecylbenzenesulfonate vesicles. *Langmuir.* **2005**, *21* (14), 6210−9.
(32) Cooper, G. M. In *The Cell: A molecular approach*, 2nd ed.; Sinauer Associates, Sunderland, Massachusetts, U.S.; 2000.
(33) Roe, D. R.; Cheatham, T. E., 3rd. PTRAJ and CPPTRAJ: software for processing and analysis of molecular dynamics trajectory data. *J. Chem. Theory Comput.* **2013**, *9* (7), 3084−95.
(34) Schneider, C. A.; Rasband, W. S.; Eliceiri, K. W. NIH Image to ImageJ: 25 years of image analysis. *Nat. Methods.* **2012**, *9* (7), 671−5.
(35) Hossain, M. S.; Berg, S.; Bergström, C. A. S.; Larsson, P. Aggregation behavior of medium chain fatty acids studied by coarse-grained molecular dynamics simulation. *AAPS PharmSciTechnol.* **2019**, *20* (2), 61.
(36) Chovancova, E.; Pavelka, A.; Benes, P.; Strnad, O.; Brezovsky, J.; Kozlikova, B.; et al. CAVER 3.0: a tool for the analysis of transport pathways in dynamic protein structures. *PLoS Comput. Biol.* **2012**, *8* (10), No. e1002708.
(37) Izrailev, S.; Stepaniants, S.; Isralewitz, B.; Kosztin, D.; Lu, H.; Molnar, F.; Wriggers, W.; Schulten, K. Steered molecular dynamics. In *Computational molecular dynamics: challenges, methods, ideas*; Springer, Berlin, Heidelberg, 1999; Vol. *4*, p 39−65. .
(38) Jarzynski, C. Nonequilibrium equality for free energy differences. *Phys. Rev. Lett.* **1997**, *78* (14), 2690−3.
(39) Bureau, H. R.; Merz, D. R., Jr.; Hershkovits, E.; Quirk, S.; Hernandez, R. Constrained unfolding of a helical peptide: implicit versus explicit solvents. *PLoS One.* **2015**, *10* (5), No. e0127034.
(40) Homeyer, N.; Stoll, F.; Hillisch, A.; Gohlke, H. Binding free energy calculations for lead optimization: assessment of their accuracy in an industrial drug design context. *J. Chem. Theory Comput.* **2014**, *10* (8), 3331−44.
(41) Izrailev, S.; Crofts, A. R.; Berry, E. A.; Schulten, K. Steered molecular dynamics simulation of the Rieske subunit motion in the cytochrome bc(1) complex. *Biophys. J.* **1999**, *77* (4), 1753−68.
(42) Grossfield, A. WHAM: the weighted histogram analysis method, version 2.0.9. http://membrane.urmc.rochester.edu/content/wham/.
(43) Zhu, F.; Hummer, G. Convergence and error estimation in free energy calculations using the weighted histogram analysis method. *J. Comput. Chem.* **2012**, *33* (4), 453−65.
(44) Biedermannova, L.; Prokop, Z.; Gora, A.; Chovancova, E.; Kovacs, M.; Damborsky, J.; et al. A single mutation in a tunnel to the active site changes the mechanism and kinetics of product release in haloalkane dehalogenase LinB. *J. Biol. Chem.* **2012**, *287* (34), 29062−74.
(45) Greene, D.; Qi, R.; Nguyen, R.; Qiu, T.; Luo, R. Heterogeneous dielectric implicit membrane model for the calculation of MMPBSA binding free energies. *J. Chem. Inf. Model.* **2019**, *59* (6), 3041−56.
(46) Miller, B. R., 3rd; McGee, T. D., Jr.; Swails, J. M.; Homeyer, N.; Gohlke, H.; Roitberg, A. E. MMPBSA.py: an efficient program for end-state free energy calculations. *J. Chem. Theory Comput.* **2012**, *8* (9), 3314−21.

https://doi.org/10.1021/jacsau.3c00725
JACS Au 2024, 4, 958−973

(47) Hac-Wydro, K.; Wydro, P. The influence of fatty acids on model cholesterol/phospholipid membranes. *Chem. Phys. Lipids.* **2007**, *150* (1), 66−81.
(48) Caliskan, M.; Poschmann, G.; Gudzuhn, M.; Waldera-Lupa, D.; Molitor, R.; Strunk, C. H.; et al. *Pseudomonas aeruginosa* responds to altered membrane phospholipid composition by adjusting the production of two-component systems, proteases and iron uptake proteins. *Biochim. Biophys. Acta Mol. Cell Biol. Lipids.* **2023**, *1868*, 159317.
(49) Papackova, Z.; Cahova, M. Fatty acid signaling: the new function of intracellular lipases. *Int. J. Mol. Sci.* **2015**, *16* (2), 3831−55.
(50) Weiler, A. J.; Spitz, O.; Gudzuhn, M.; Schott-Verdugo, S. N.; Kamel, M.; Thiele, B.; et al. A phospholipase B from *Pseudomonas aeruginosa* with activity towards endogenous phospholipids affects biofilm assembly. *Biochim. Biophys. Acta Mol. Cell. Biol. Lipids.* **2022**, *1867* (4), 159101.
(51) Berman, H. M.; Westbrook, J.; Feng, Z.; Gilliland, G.; Bhat, T. N.; Weissig, H.; et al. The protein data bank. *Nucleic Acids Res.* **2000**, *28* (1), 235−42.
(52) Sali, A.; Blundell, T. L. Comparative protein modelling by satisfaction of spatial restraints. *J. Mol. Biol.* **1993**, *234* (3), 779−815.
(53) Murzyn, K.; Rog, T.; Pasenkiewicz-Gierula, M. Phosphatidylethanolamine-phosphatidylglycerol bilayer as a model of the inner bacterial membrane. *Biophys. J.* **2005**, *88* (2), 1091−103.
(54) Martinez, L.; Andrade, R.; Birgin, E. G.; Martinez, J. M. PACKMOL: a package for building initial configurations for molecular dynamics simulations. *J. Comput. Chem.* **2009**, *30* (13), 2157−64.
(55) Schott-Verdugo, S.; Gohlke, H. PACKMOL-Memgen: A simple-to-use, generalized workflow for membrane-protein-lipid-bilayer system building. *J. Chem. Inf. Model.* **2019**, *59* (6), 2522−8.
(56) Pashkovskaya, A. A.; Vazdar, M.; Zimmermann, L.; Jovanovic, O.; Pohl, P.; Pohl, E. E. Mechanism of long-chain free fatty acid protonation at the membrane-water interface. *Biophys. J.* **2018**, *114* (9), 2142−51.
(57) Salomon-Ferrer, R.; Gotz, A. W.; Poole, D.; Le Grand, S.; Walker, R. C. Routine microsecond molecular dynamics simulations with AMBER on GPUs. 2. Explicit solvent particle mesh ewald. *J. Chem. Theory Comput.* **2013**, *9* (9), 3878−88.
(58) Maier, J. A.; Martinez, C.; Kasavajhala, K.; Wickstrom, L.; Hauser, K. E.; Simmerling, C. ff14SB: Improving the accuracy of protein side chain and backbone parameters from ff99SB. *J. Chem. Theory Comput.* **2015**, *11* (8), 3696−713.
(59) Dickson, C. J.; Madej, B. D.; Skjevik, A. A.; Betz, R. M.; Teigen, K.; Gould, I. R.; et al. Lipid14: The amber lipid force field. *J. Chem. Theory Comput.* **2014**, *10* (2), 865−79.
(60) Dickson, C. J.; Walker, R. C.; Gould, I. R. Lipid21: complex lipid membrane simulations with AMBER. *J. Chem. Theory Comput.* **2022**, *18* (3), 1726−36.
(61) Zhao, C. L.; Zhao, D. X.; Bei, C. C.; Meng, X. N.; Li, S.; Yang, Z. Z. Seven-site effective pair potential for simulating liquid water. *J. Phys. Chem. B* **2019**, *123* (21), 4594−603.
(62) Li, P.; Song, L. F.; Merz, K. M., Jr. Systematic parameterization of monovalent ions employing the nonbonded model. *J. Chem. Theory Comput.* **2015**, *11* (4), 1645−57.
(63) Sengupta, A.; Li, Z.; Song, L. F.; Li, P.; Merz, K. M., Jr. Correction to ″Parameterization of monovalent ions for the OPC3, OPC, TIP3P-FB, and TIP4P-FB water models″. *J. Chem. Inf. Model.* **2021**, *61* (7), 3734−5.
(64) Krautler, V.; Van Gunsteren, W. F.; Hunenberger, P. H. A fast SHAKE: Algorithm to solve distance constraint equations for small molecules in molecular dynamics simulations. *J. Comput. Chem.* **2001**, *22* (5), 501−8.
(65) Le Grand, S.; Gotz, A. W.; Walker, R. C. SPFP: Speed without compromise-A mixed precision model for GPU accelerated molecular dynamics simulations. *Comput. Phys. Commun.* **2013**, *184* (2), 374−80.
(66) Quigley, D.; Probert, M. I. Langevin dynamics in constant pressure extended systems. *J. Chem. Phys.* **2004**, *120* (24), 11432−41.
(67) Berendsen, H. J. C.; Postma, J. P. M.; van Gunsteren, W. F.; DiNola, A.; Haak, J. R. Molecular dynamics with coupling to an external bath. *J. Chem. Phys.* **1984**, *81* (8), 3684−3690.
(68) Lin, Y.; Pan, D.; Li, J.; Zhang, L.; Shao, X. Application of Berendsen barostat in dissipative particle dynamics for nonequilibrium dynamic simulation. *J. Chem. Phys.* **2017**, *146* (12), 124108.
(69) Marrink, S.-J.; Berger, O.; Tieleman, P.; Jahnig, F. Adhesion forces of lipids in a phospholipid membrane studied by molecular dynamics simulations. *Biophys. J.* **1998**, *74* (2), 931−943.
(70) Schymkowitz, J.; Borg, J.; Stricher, F.; Nys, R.; Rousseau, F.; Serrano, L. The FoldX web server: an online force field. *Nucleic Acids Res.* **2005**, *33*, W382.
(71) Guerois, R.; Nielsen, J. E.; Serrano, L. Predicting changes in the stability of proteins and protein complexes: a study of more than 1000 mutations. *J. Mol. Biol.* **2002**, *320* (2), 369−87.
(72) Tokuriki, N.; Stricher, F.; Schymkowitz, J.; Serrano, L.; Tawfik, D. S. The stability effects of protein mutations appear to be universally distributed. *J. Mol. Biol.* **2007**, *369* (5), 1318−32.
(73) Subrini, O.; Sotomayor-Perez, A. C.; Hessel, A.; Spiaczka-Karst, J.; Selwa, E.; Sapay, N.; et al. Characterization of a membrane-active peptide from the Bordetella pertussis CyaA toxin. *J. Biol. Chem.* **2013**, *288* (45), 32585−98.
(74) Kovacic, F.; Bleffert, F.; Caliskan, M.; Wilhelm, S.; Granzin, J.; Batra-Safferling, R.; et al. A membrane-bound esterase PA2949 from *Pseudomonas aeruginosa* is expressed and purified from Escherichia coli. *FEBS Open Bio.* **2016**, *6* (5), 484−93.
(75) Bertani, G. Studies on lysogenesis. I. The mode of phage liberation by lysogenic Escherichia coli. *J. Bacteriol.* **1951**, *62* (3), 293−300.
(76) Laemmli, U. K. Cleavage of structural proteins during the assembly of the head of bacteriophage T4. *Nature.* **1970**, *227* (5259), 680−5.
(77) Ritchie, T. K.; Grinkova, Y. V.; Bayburt, T. H.; Denisov, I. G.; Zolnerciks, J. K.; Atkins, W. M.; et al. Chapter 11 - Reconstitution of membrane proteins in phospholipid bilayer nanodiscs. *Methods Enzymol.* **2009**, *464*, 211−31.
(78) Jaeger, K. E.; Kovacic, F. Determination of lipolytic enzyme activities. *Methods Mol. Biol.* **2014**, *1149*, 111−34.
(79) Jayachandra, K.; Gowda, M. D. M.; Rudresha, G. V.; Manjuprasanna, V. N.; Urs, A. P.; Nandana, M. B.; et al. Inhibition of sPLA(2) enzyme activity by cell-permeable antioxidant EUK-8 and downregulation of p38, Akt, and p65 signals induced by sPLA(2) in inflammatory mouse paw edema model. *J. Cell. Biochem.* **2023**, *124* (2), 294−307.
(80) Mahmood, T.; Yang, P. C. Western blot: technique, theory, and trouble shooting. *N. Am. J. Med. Sci.* **2012**, *4* (9), 429−34.
(81) Urbani, A.; Warne, T. A colorimetric determination for glycosidic and bile salt-based detergents: applications in membrane protein research. *Anal. Biochem.* **2005**, *336* (1), 117−24.

https://doi.org/10.1021/jacsau.3c00725
JACS Au 2024, 4, 958−973